Implementation of Acuros XB Dose Calculation in to Clinical Radiation Therapy Workflows

by

Brett G. Erickson

Graduate Program in Medical Physics
Duke University

Date: _____

Approved:

_____
Justus Adamson, Supervisor

_____
Yunfeng Cui

_____
Christopher Kelsey

A thesis submitted in partial fulfillment of the
requirements for the degree of Master of Science
in the Graduate Program in Medical Physics
in the Graduate School of
Duke University

2022

ABSTRACT

Implementation of Acuros XB Dose Calculation in to Clinical Radiation Therapy Workflows

by

Brett G. Erickson

Graduate Program in Medical Physics
Duke University

Date: _____

Approved:

_____
Justus Adamson, Supervisor

_____
Yunfeng Cui

_____
Christopher Kelsey

An abstract of a thesis submitted in partial fulfillment of the
requirements for the degree of Master of Science
in the Graduate Program in Medical Physics
in the Graduate School of
Duke University

2022

Abstract

Stereotactic body radiation therapy (SBRT) is a common treatment technique that can be used to treat tumors for multiple cancer sites. Density heterogeneity in the target volume and beam path combined with small treatment fields has made dose calculation in lung SBRT difficult. Dose calculation algorithms used historically have difficulty modelling the extreme density heterogeneity present in lung SBRT and have been shown to overestimate the dose delivered to tumors situated in the lung parenchyma. Recently, more advanced algorithms that directly model heterogeneity have been implemented for clinical treatment planning. The limited accuracy of historically utilized dose calculation algorithms has raised questions about their effects on local control due to the possibility of tumor underdosing. The first part of this work establishes a proper dose normalization technique when implementing these advanced algorithms for treatment planning in order to keep consistent radiation beam settings and to quantify the dosimetric effect of various dose normalizations. The second aim is to quantify the effects dosimetric accuracy has on local control in lung SBRT.

To investigate proper dose normalization, 87 lung SBRT plans with doses originally calculated with the Anisotropic Analytical Algorithm (AAA) had their doses recalculated with the new Acuros XB (AXB) algorithm, which is able to directly model the heterogeneity of the lungs and treatment volume. After recalculation, the plan was normalized to the planning target volume (PTV) D95%, internal target volume (ITV) D99%, and to match the original PTV coverage. The percentage change in total monitor units (MU) between the AXB renormalized plans and the original AAA plans were calculated to quantify how the delivered radiation would change when implementing the AXB algorithm for lung SBRT treatment planning. Percentage changes in relevant PTV and ITV dose metrics as well as absolute changes in relevant organ at risk (OAR) dose metrics were quantified to compare plan dosimetry. OAR doses were compared to the current institutional planning objectives to investigate the feasibility of meeting the current objectives with the new algorithm.

To investigate the effect of dosimetric accuracy on local control, 162 patients previously treated with SBRT were selected from a retrospective protocol comparing the efficacy of SBRT and surgery for treatment of early-stage non-small cell lung cancer. Plans had their doses originally computed

with the Pencil Beam Convolution (PBC, $n = 8$) algorithm or AAA ($n = 156$). Each plan was recalculated with AXB with identical beam settings. A subset was also recalculated with Monte Carlo to validate the accuracy of the AXB calculations. Percentage changes in relevant PTV and ITV biologically effective doses (BED) were calculated between the original and AXB plans to quantify the magnitude of the dosimetric differences between the old and new algorithm. A multivariable linear regression was performed to investigate which patient and treatment parameters influenced the magnitude of these dosimetric changes. A competing risk analysis was performed to quantify the association between the magnitude of the dosimetric changes and local failure.

Normalizing the AXB plan to the PTV D95% and keeping the original PTV coverage typically resulted in a total MU increase (average increase of 7.0% and 7.9%, respectively) while normalizing to the ITV D99% resulted in similar total MU (average increase of 0.31%). When normalizing to the PTV D95%, the AXB plans had increased PTV and ITV D1%[Gy] (median increases of 3.4% and 3.2%, respectively) while normalizing to the ITV D99% showed a median 1.9% decrease. Normalizing the AXB plans to the PTV D95% typically resulted in increased OAR dose for all OARs and an inferior ability to meet the OAR planning constraints. Reoptimization of the renormalized plans showed the current OAR objectives to be manageable when using the AXB algorithm.

The AXB dose calculations were much more consistent with Monte Carlo than were the original dose calculations. A large range of dosimetric decreases upon recalculation with AXB were observed for both patients who failed locally and those who were controlled. Higher beam energy was found to increase the magnitude of the dosimetric decreases (expected decrease in PTV mean BED of 3.6%, 5.9%, and 9.1% when using 6X, 10X, or 15X, respectively). Total lung volume was also associated with an increased magnitude of dosimetric decrease (expected decerease of 0.8% per 500 cc for the PTV mean BED). The median follow-up time of the cohort was 26 months. 15 patients experienced local failures. Upon univariate analysis, the dosimetric decreases in the PTV and ITV D1% BED were found to be associated with local failure (hazard ratio (HR) of 0.89 (p=0.04) and 0.87 (p=0.02), respectively). Upon multivariate analysis, the dosimetric decrease in the ITV D1% BED remained significant when controlling for PTV volume (HR=0.89 (p=0.04)).

More accurate dose calculation algorithms are beginning to be implemented for clinical treat-

ment planning. When implementing these new algorithms, issues arise with dose normalization due to the potential for vast differences between the dose distributions calculated with the different algorithms. Normalizing the dose to the PTV D95% in the AXB plan will result in a delivered dose increase relative to a AAA plan while normalizing to the ITV D99% will keep similar delivered doses between the plans. Dose metrics typically increase when normalizing to the PTV D95% (for targets and OARs) while normalizing to the ITV D99% typically decreased the reported dose metrics. The OAR planning objectives are manageable using the AXB algorithm.

Many factors are related to the magnitude of the dosimetric decreases observed when recalculating plans with AXB, including but not limited to beam energy and lung volume. Most of the dose differences investigated were not associated with local failure, but the change in the PTV and ITV D1% BEDs were found to be associated with local failure in the univariate analysis.

Contents

List of Tables

List of Figures

List of Abbreviations

AAA - Anisotropic Analytical Algorithm

AXB - Acuros XB

BED - biologically effective dose

BH - breath-hold

CCC - Collapsed Cone Convolution

CI - confidence interval

CT - computed tomography

FB - free breathing

FS - field size

GTV - gross tumor volume

HIGRT - hypofractionated image-guided radiation therapy

HR - hazard ratio

HU - Hounsfield unit

HVL - half-value layer

IMRT - intensity modulated radiation therapy

IRB - institutional review board

ITV - internal target volume

KM - Kaplan-Meier

LBTE - linear Boltzmann transport equation

LQ - linear-quadratic

MLC - multileaf collimator

MU - monitor units

MV - megavoltage

MVA - multivariate analysis

NSCLC - non-small cell lung cancer

OAR - organ at risk

PB - pencil beam

PBC - Pencil Beam Convolution

PTV - planning target volume

RTOG - Radiation Therapy Oncology Group

SBRT - stereotactic body radiation therapy

SMC - SciMoCa

TCP - tumor control probability

TERMA - total energy released per unit mass

TMR - tissue maximum ratio

TPR - tissue phantom ratio

TPS - treatment planning system

UVA - univariate analysis

VMAT - volumetric modulated arc therapy

3DCRT - 3-dimensional conformal radiation therapy

4DCT - 4-dimensional computed tomography

Acknowledgements

I would like to extend my gratitude to Dr. Justus Adamson for his continued guidance and support. It was a pleasure to be able to work under you. I would also like to thank Dr. Yunfeng Cui for co-advising me. It was great to have you on board with my project and I appreciated the time you took out of your day to teach me. You both have taught me what it takes to perform good research. You both were nothing but supportive during my time and I feel very fortunate to have learned from both of you. I feel so lucky to have been able to work on this project and I will take all of the lessons I have learned along the way with me wherever I go. Thank you for being patient and willing to answer my stupid questions.

To Dr. Chris Kelsey, I appreciate the time you put in to serving on my thesis committee. It was great being able to learn from you and I appreciate you sharing your clinical expertise with me. To Brad Ackerson, thank you for teaching me the value of working in a team. One of the most rewarding aspects of this project was to work with such a wide variety of clinicians. Interacting with you both has taught me a valuable lesson in teamwork, and radiation oncology is one of those fields where you simply can't function without a team of excellent clinicians. You both are no exception to the "excellent" phrase and I feel very fortunate to have learned from both of you.

I would like to also thank my family for their support of my endeavors. You have always believed in me and told me I could be anything I want to be. If you would have told me 10 years ago if I would be graduating from Duke with a medical physics degree, I would first asked "What in the world is medical physics?" and then I would have looked at you and told you that you were crazy. Yet here we are.

To my lovely girlfriend, Sophie, where would I be without you. You have been nothing but supportive of me during my studies and all of my busy days with interviews and what not. Thank you for your patience and willingness to come visit me in Durham. I appreciate your support more than you know, and I truly do not think I would be in the situation I am currently in if it weren't for you. For that I will be forever grateful.

And lastly, to my amazing classmates: thank you for making this journey a great one. I will

never forget any of you, from our very first math workshop class together to when we finally get handed that degree title. I have made many friendships along the way and intend to keep them. I wish you all the best.

Chapter 1

Dose Calculation Algorithms in Radiation Therapy

The purpose of radiation therapy is to deliver a high radiation dose to diseased areas while minimizing the dose delivered to normal tissues or structures, all in an effort to increase the therapeutic ratio. Many advancements in radiation oncology have worked towards increasing the therapeutic ratio, many of which can be attributed to the vast increase in computing power in past decades. Many important steps are needed in the process of producing quality radiation therapy treatment plans. One of the most critical elements of any treatment plan is the calculated dose distribution, which gives the planner and treating physician a direct representation of the therapeutic ratio. Accurate dose calculation in radiation therapy is essential in assuring physicians their prescribed treatment doses are properly fulfilled.

1.1 Clinical Dose Calculation Algorithms

Many commercial dose calculation algorithms are available for clinical treatment planning. Each algorithm has its own advantages and disadvantages, a few being computation speed and calculation accuracy. Dose calculation algorithms can broadly be categorized in to three distinct groups [1]:

- Type A algorithms: algorithms that do not consider the lateral changes in electron transport in the presence of heterogeneities (pencil beam algorithms)

- Type B algorithms: algorithms that imprecisely consider the lateral changes in electron transport and scale accordingly in different directions (convolution/superposition algorithms)

- Type C algorithms: algorithms rigorously accounting for the physics and probabilistic nature of dose absorption (linear Boltzmann transport equation (LBTE) solvers and Monte Carlo simulations)

The three types of algorithms fundamentally differ in their approach to dose calculation. Earlier and more primitive models are considered type A algorithms while more advanced and modern algorithms are considered to be type B or C algorithms, depending on level of rigor. Monte Carlo dose calculation is considered the gold standard in radiation therapy as it has proven to be the most consistent with dose measurements, but the computational demands of Monte Carlo calculations make it infeasible for most routine clinical situations. Over time, technological advancement and enhanced computing power has allowed for more accurate and faster dose calculation, which has greatly improved normal tissue sparing and tumor control in radiation therapy. The mathematical basis of each algorithm will be explored in detail next.

1.1.1 Pencil Beam Dose Calculation

Several models of pencil beam dose calculation have been implemented for clinical treatment planning [2, 3, 4]. The pencil beam (PB) model developed by Nyholm et al. [3] will be presented here. Note that this only represents one implementation of the pencil beam algorithm. However, similar approaches are used in other pencil beam implementations. Generally, PB calculation algorithms involve a two-dimensional integration of an energy deposition kernel over the energy fluence at a given depth. This type of dose calculation relies on measured beam data in order to realistically model photon energy deposition.

General Principles

In essence, the pencil beam model of dose calculation uses a simplified 2-D dose kernel found by analytical fitting to Monte Carlo simulation results. The energy fluence distribution impinging upon the patient is often estimated through measurements of the given radiation beam. The beam

model can be altered in order to more accurately represent individual photon beams. Contaminant radiation is usually accounted for with additional dose kernels. Various corrections can be added to the model to account for various physical principles, such off-axis softening and beam hardening. The general work flow of a pencil beam dose calculation algorithm is shown in Fig. 1.1. This model can be applied to any irregular field shape by taking in to account the collimated field shape and assigning points beneath a block to be without fluence.

Mathematical Formalism

By fitting Monte Carlo simulations modelling dose deposition in a homogeneous water medium to analytical functions, the pencil beam dose kernel was found to be best described by:

$$\frac{P}{\rho}(r,d) = \frac{A(d)\exp\left(-a(d)\times r\right) + B(d)\exp\left(-b(d)\times r\right)}{r} \tag{1.1}$$

which represents dosimetric contributions from the primary and scatter dose. In Eq. 1.1, $A, a, B,$ and b are depth-dependent fit parameters obtained from the kernel modelling and r is the radial distance in the calculation plane from the point of calculation to the point that is contributing dose to the calculation point. The dose kernel is considered to be circularly symmetric. For the purpose of this work, electron and photon contamination kernels will be ignored. The parameters $A, a, B,$ and b, in turn, can be calculated using the following expressions:

$$\frac{A}{a}(d) = A_1\left[1-\exp\left(A_2\sqrt{d^2+A_5^2}\right)\right]\exp\left(A_3 d + A_4 d^2\right)$$

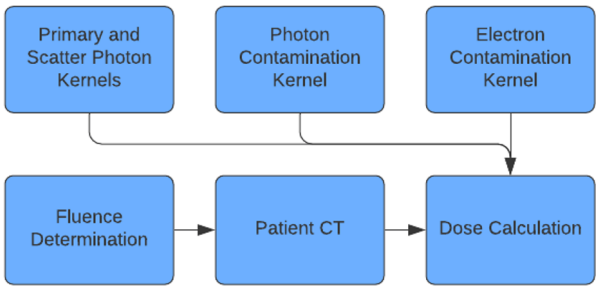

Figure 1.1: General idea of a pencil beam model. Measured beam data is combined with specific pencil beam parameters to develop a beam model, which can then be applied to the treatment geometry to calculate dose within a patient.

$$\frac{B}{b}(d) = B_1 \left[1 - \exp\left(B_2\sqrt{d^2 + B_5^2}\right)\right] \exp\left(B_3 d + B_4 d^2\right)$$

$$a(d) = a_2 + a_1 d$$

$$b(d) = b_1 \left[1 - \exp\left(b_2\sqrt{d^2 + b_5^2}\right)\right] \exp\left(b_3 d + b_4 d^2\right)$$

where $A_{1-5}, B_{1-5}, a_{1-2},$ and b_{1-5} are parameters designed to realistically model the depth dependencies of the primary and scatter dose within the medium and d is the depth of calculation in the patient. Each of these parameters are dependent on a beam quality specifier unique to each radiation beam. In this specific implementation, the relationship between these parameters and the beam quality specifier follows a 5th order polynomial and is given by:

$$P_i = \sum_{j=0}^{j=5} C_{j,P_i} \left(\frac{\text{TMR(FS=10, } d = 20)}{\text{TMR(FS=10, } d = 10)}\right)^j$$

where P_i is the ith parameter (17 total), C_{j,P_i} is the jth fit value (6 per parameter) for the ith parameter (fit values are obtained from the literature), and TMR(FS, d) is the tissue-maximum ratio at the specified field size (FS) and depth (d) (this ratio of TMR values is also known as the $\text{TPR}_{20/10}$, the tissue-phantom ratio). Each of the parameters in the dose kernel realistically models different physical phenomena, such as the buildup region and the beam hardening effect. Note that other pencil beam models may utilize different beam quality indices to characterize the dose kernel.

Dose Calculation

To get the total dose delivered to a single point, a two-dimensional integration is performed around the calculation point, hence accounting for the dosimetric contributions to the calculation point from all other points within the field lying in the same plane as the calculation point. The geometry for an arbitrary field shape is shown in Fig. 1.2. Mathematically, this is accomplished by integrating Eq. 1.1 multiplied by the energy fluence over all points where there is fluence:

$$D(x,y) = \int_0^{2\pi} \int_0^{r_{max}} \frac{A(d)\exp\left(-a(d)\times r\right) + B(d)\exp\left(-b(d)\times r\right)}{r} \cdot \Psi(r,\theta) \cdot r dr d\theta \quad (1.2)$$

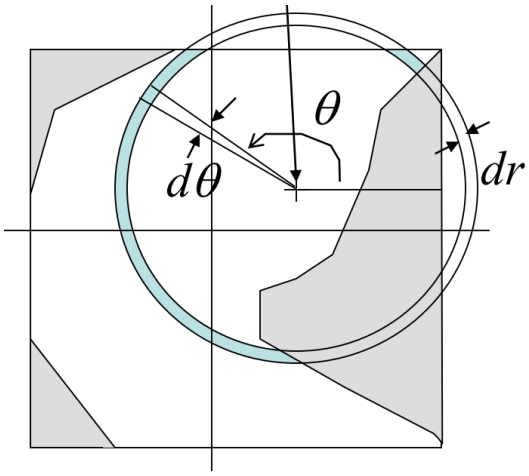

Figure 1.2: **Geometry used for a pencil beam dose computation. Contributions from each point in the collimated field are summed to yield the dose at the calculation point.**

In Eq. 1.2, r_{max} represents the maximum circular radius in which there will be fluence and $\Psi(r, \theta)$ represents the energy fluence at radial position r and angular position θ relative to the point of calculation (x, y). Note that if the contribution point specified by $(r,\ \theta)$ is beneath a block, the energy fluence at the point will be 0 and no dose is contributed to the calculation point from that particular location. Equation 1.2 can be used to calculate the dose to any point with any field shape. There is usually no analytical solution to this integral, so computational methods are used to estimate its value. Physically, the integral represents the individual contributions to the dose at the calculation point from all other points within the collimated radiation field. Of note, this is a planar integral; it is a two-dimensional integration over the radiation field at the given calculation depth. To get the dose at all depths in the patient, the same expression may be applied to each depth, which will alter the dose kernel due to the depth dependence of the pencil beam parameters. Once the integration is applied to all depths, a volumetric dose distribution may be reconstructed by stacking the individual dose planes.

If we assume the field aperture to be circularly symmetric with radius R and constant planar energy fluence Ψ, we can carry out the integration in Eq. 1.2 and get the dose to the center of a circular field of radius R at depth d:

$$D(R,d) = 2\pi\Psi\left[\frac{A}{a}(d)\left[1-\exp\left(-a(d)R\right)\right] + \frac{B}{b}(d)\left[1-\exp\left(-b(d)R\right)\right]\right] \tag{1.3}$$

Equation 1.3 only works for circular fields along the central axis. However, this equation can also be applied to rectangular fields by calculating an approximate equivalent circular field radius. The equation to calculate the equivalent circular field radius is shown below:

$$R_{eq} = 0.561 \times \frac{4A}{P}$$

where A is the area of the rectangular field and P is the perimeter of said field. This value can be substituted for R in Eq. 1.3, hence allowing for application of Eq. 1.3 to rectangular field shapes. If the field shape is irregular, approximations can be made to determine an equivalent rectangular field shape and then an equivalent circular field radius may be computed.

Fluence Determination

The fluence used in the PB dose calculation formalism can be determined using the linear accelerator calibration condition. After calibrating a specific linear accelerator according to acceptable protocols (such as the American Association of Physicists in Medicine Task Group 51 [5]), the known dose under calibration conditions can be used to estimate the energy fluence by using Eq. 1.3. Once the energy fluence for the calibration condition is determined, an inverse square correction can be applied for any source-to-calculation-plane distance to determine the energy fluence at the correct depth. Note that other factors, such as attenuation and irregular field shapes, are accounted for in the pencil beam model itself.

Off-Axis Softening

Due to the nature of x ray production in the treatment head, the energy fluence distribution across a given calculation plane perpendicular to the central axis is not constant. The angular distribution of x rays emanating from the x-ray target is forward peaked for clinical MV photon beams. Because of this, a flattening filer is often placed in the beam in order to flatten the photon spectrum. The flattening filter is designed to differentially attenuate the photon beam by absorbing more photons near the center of the beam and absorbing less photons near the edge. This results in a harder beam near the center and a softer beam near the beam edges. To account for this ”off-axis softening,”

the beam quality index used to model the dose kernel ($\text{TPR}_{20/10}$) is altered according to the off-axis half-value layer (HVL). The HVL gets lower the further off-axis the calculation point is due to the beam softening effect. Therefore, the beam quality index at points off-axis is also lower since the beam has less pentrating power. Empirical relations exist between the HVL and beam quality indices [6], so by determining the HVL at all points off-axis, the corresponding off-axis beam quality index may also be calculated. The HVL can be computed at points defined by off-axis angle ϕ using the following equation:

$$\text{HVL}(\phi) = \frac{\text{HVL}(0)}{1 + d_1\phi + d_2\phi^2 + d_3\phi^3} \tag{1.4}$$

where d_{1-3} are empirical fit parameters given in the paper by Nyholm et al [6], ϕ is the off-axis angle measured from the central axis, and $\text{HVL}(0)$ is the HVL along the central axis. Once this is computed, an empirical relationship exists between the HVL and the $\text{TPR}_{20/10}$:

$$\text{TPR}_{20/10} = -\frac{a_2}{2a_3} + \sqrt{\left(\frac{a_2}{2a_3}\right)^2 - \frac{a_1 - \text{HVL}}{a_3}} \tag{1.5}$$

where a_{1-3} are fit parameters taken from Nyholm et al. [6]. The $\text{TPR}_{20/10}$ is a quadratic function of the HVL, but we only take the positive root since the negative root yields an unrealistic value for the $\text{TPR}_{20/10}$. $\text{HVL}(0)$ can be calculated by inverting Eq. 1.5 and using the measured TMR values to compute the $\text{TPR}_{20/10}$. Changing the $\text{TPR}_{20/10}$ at each off-axis point consequently changes the pencil beam parameters at each off-axis point due to the relationship between the pencil beam parameters and the $\text{TPR}_{20/10}$. The energy fluence is considered to be constant at a given planar depth and off-axis softening is accounted for by altering the beam quality index.

Heterogeneity Correction

The calculated dose up to this point has assumed a homogeneous water medium. While patient interiors may be nearly water equivalent in some cases, the presence of different density tissues (such as bone, air, and tissue interfaces) can significantly alter the actual delivered dose due to distortion of the dose deposition kernels and changing energy fluence. Modelling heterogeneity in pencil beam models is extremely difficult as the integration is done over a plane at the calculation

depth. The corrections applied in a PB model involve the use of the radiological depth, which can be calculated from the patient's computed tomography (CT) dataset. The radiological depth is defined as the actual depth scaled by the average attenuation coefficient relative to water along the pencil beam path. The radiological depth at each point in the medium is used to derive a unique scaling factor for each corresponding dose voxel, but only takes in to account heterogeneity along the direction of propagation. This heterogeneity correction does not consider changes in penumbra width or lack of scatter equilibrium observed in low density regions or interfaces, which may adversely affect the accuracy of the calculation. This correction also does not consider the chemical makeup of different materials. Higher or lower density tissues are represented as water with varying densities calculated from the voxel Hounsfield unit.

Other Implementations

This is one implementation of pencil beam dose computation. The pencil beam parameters in this model are developed for use with measured $\text{TPR}_{20/10}$ values, which are unique to each radiation beam. In addition, the energy fluence along the central axis is calculated from the cirucular field approximation shown in Eq. 1.3 using the accelerator calibration condition. Off-axis softening is accounted for by calculating the $\text{TPR}_{20/10}$ at off-axis points. While including these various correction factors enhances the calculation accuracy, calculation speed is reduced. The models can get as sophisticated as the user pleases, but one must keep in mind the tradeoff between calculation accuracy and calculation time. Other beam measurements may be used to characterize radiation beams, both in regards to the dose kernels and the energy fluence determination.

1.1.2 Convolution-Superposition Dose Calculation

Many convolution-superposition algorithms have been developed and are currently in use for clinical treatment planning [7, 8, 9]. The method outlined by Papanikolaou et al. [8] is reviewed here. Generally, convolution-superposition models employ a 3-D convolution technique to model energy deposition within a patient geometry.

General Principles

Convolution-superposition models make use of Monte Carlo derived dose spread arrays that can be applied to a given treatment geometry to compute dose for any patient geometry. The dose spread arrays, or dose kernels, are usually derived in homogeneous water phantoms. Dose contributions from different sources, such as photon or electron contamination, can be divided in to separate kernels and added together to get the total dose to a voxel. The general convolution-superposition workflow is shown in Fig. 1.3.

Mathematical Formalism

Doses computed with the convolution-superposition method make use of the distribution of total energy released per unit mass (TERMA) within the patient convolved with the total dose kernel. In practice, the dose kernels are divided in to a primary dose kernel resulting from primary interactions and secondary dose kernels resulting from scattered particle interactions. Generally, the energy fluence spectrum at depth d is given by

$$\frac{d\Psi}{dh\nu}(\vec{r}, h\nu) = h\nu e^{-\mu(h\nu)d} \left(\frac{|\ \vec{r_0}\ |}{|\ \vec{r}\ |} \right)^2 \frac{d\Phi_0}{dh\nu}(h\nu) \tag{1.6}$$

where $\vec{r} = (x, y, z)$ is the spatial position vector, $h\nu$ is the photon energy, μ is the linear attenuation coefficient for the medium at the given energy, d is the path length travelled through tissue, $\vec{r_0}$ is the location at the surface of the phantom from which we calculate the inverse square correction, and $\frac{d\Phi_0}{dh\nu}(h\nu)$ is the initial number fluence spectrum prior to entering the patient. The inverse

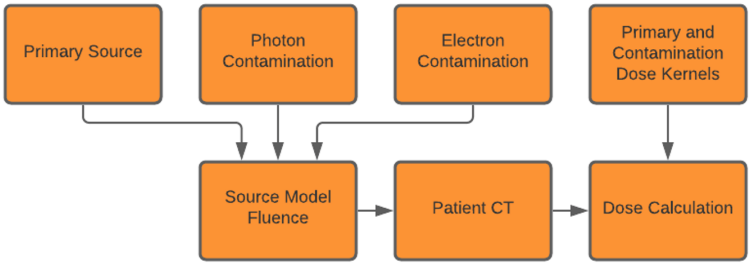

Figure 1.3: **General idea for a convolution-superposition algorithm. Monte Carlo derived dose kernels are combined with measured beam data to develop a beam model, which can then be used to compute radiation dose to any treatment geometry.**

square factor here is a simplification in that it is applied to each voxel individually. To produce a more realistic situation, the dose kernel used in the dose computation should be tilted to match the direction of propagation for each beam path through the patient, although this operation greatly increases the computation time. However, this simplified correction produces reasonable agreement with measurements. The TERMA can then be calculated by integrating Eq. 1.6 multiplied by the mass attenuation coefficient:

$$T(\vec{r'}, \text{MV}) = \int \frac{\mu}{\rho}(h\nu)\frac{d\Psi}{dh\nu}(\vec{r'}, h\nu)dh\nu \tag{1.7}$$

where $T(\vec{r'}, \text{MV})$ is the TERMA at point $\vec{r'}$ for the energy spectrum defined by the nominal beam energy MV and $\frac{\mu}{\rho}(h\nu)$ is the energy-dependent mass attenuation coefficient of the medium. Dose kernels are often normalized per unit TERMA, so the TERMA distribution within the patient must be known prior to dose calculation. Since the incident photon energy spectrum is normally approximated through discrete Monte Carlo calculations, the above integrals can be approximated by calculating average values for all energy-dependent parameters accounting for the energies and relative weights present in the photon energy spectrum. These approximations produce reasonable agreement with measurements, but sacrifice calculation accuracy for computation speed.

Dose Calculation

Once the TERMA is determined at every point within the calculation volume using Eq. 1.7, each beam can be convolved with the dose kernel normalized to unit TERMA to get the total dose within the volume (ensuring the dose kernel is properly rotated to match the orientation of each beam). Note that the TERMA distribution accounts for the beam geometry; no fluence is incident upon the patient outside of the collimated radiation field. The dose kernels are designed to give the absorbed dose to the medium per unit TERMA. Mathematically, this is represented as a three-dimensional convolution:

$$D(r) = \int T(r') \cdot A(r - r')d^3r' \tag{1.8}$$

where $D(r)$ is the dose at position definied by r and $A(r - r')$ represents the dose contribution to point r from point r' due to primary and scatter dose (i.e., the total dose kernel). Practically, the

total dose kernel is usually split in to individual kernels representing primary and scatter dose and each source of contribution is computed separately and summed together to get the total dose. Once the dose kernels are calculated using Monte Carlo, they can be stored for use with any treatment geometry. Other corrections can be made to account for varying physical effects, such as beam harding, off-axis softening, and penumbra widening in low density media.

Heterogeneity Correction

As outlined in the paper by Mackie et al. [7], O'Connor's theorem allows for the use of a single dose kernel for different density voxels. Dose kernels are typically stored for certain values of $\rho \cdot l$, where ρ is the density of the voxel from which the kernel was derived and l is the size of the voxel. O'Connor's theorem states that a dose kernel can be used for different density media as long as the product $\rho \cdot l$ is equal to the given product for the stored dose kernel. That is,

$$\rho_{med} \cdot l_{med} = \rho_{\text{stored}} \cdot l_{\text{stored}}$$

where ρ_{med} and l_{med} are the density derived from the CT dataset and the CT voxel size, respectively. For example, by O'Connor's theorem, the same dose kernel may be used for a medium with density 1 g/cc and voxel size 1 cm and a medium with density 0.2 g/cc and voxel size 5 cm. This kernel scaling provides reasonable accuracy in low density regions where penumbral widening is an issue. This scaling of the dose kernel allows for better representation of heterogeneous media compared to the pencil beam formalism since the kernel can be scaled in multiple directions, thereby partially accounting for changes in lateral electron scatter rather than just along the depth direction. In addition, the energy fluence distribution (and hence TERMA) may be scaled according to local density variations defined by the CT dataset, which also serves to alter the dose distribution in the presence of heterogeneity. These correction gives better results at tissue interfaces, but modelling tissue interfaces still proves difficult. The chemical composition of the medium is usually not taken in to account as tissues are represented as water with varying density.

Other Implementations

This is one example of a convolution-superposition dose calculation algorithm. While other convolution-superposition algorithms follow similar methodologies, they primarily differ in the shape of their dose kernels and how they handle heterogeneity. For example, in the Anisotropic Analytical Algorithm (AAA), heterogeneity is accounted for in the lateral direction by scaling the dose kernel according to the local electron density in each direction. In contrast, the Collapsed Cone Convolution (CCC) algorithm surrounds each voxel with a set of radial lines emanating from the center of the voxel. These lines surround the voxel in the entire 3-D space and are able to account for heterogeneity along each line by employing a cone-shaped scatter kernel along each line that is scaled according to local density variations. Each implementation provides reasonable accuracy in the presence of heterogeneities.

1.1.3 Dose Calculation Using LBTE Solvers

The method of using LBTE solvers to calculate dose has been explained by Vassiliev et al. [10] and will be reviewed here. In addition, Bedford has reviewd the use of LBTE solvers in radiation therapy dose calculation [11].

General Principles

LBTE solvers are a deterministic approach to dose calculation and calculate the dose by discretely solving the coupled LBTE for the photon and electron transport in the calculation volume. The LBTE is a series of complex intero-differential equations accounting for all possible radiation interactions, including the photoelectric effect, Compton scattering, pair production, and the Coulombic interactions between charged particles and the atoms in the medium. The LBTE is solved in an iterative fashion by considering the conservation of angular electron and photon fluence as the radiation beam is transported through the patient. The general workflow for a gridded LBTE solver algorithm is shown in Fig. 1.4. By accounting for the various interaction patterns of radiation in human tissues, the LBTE can be solved for the photon and electron transport within the

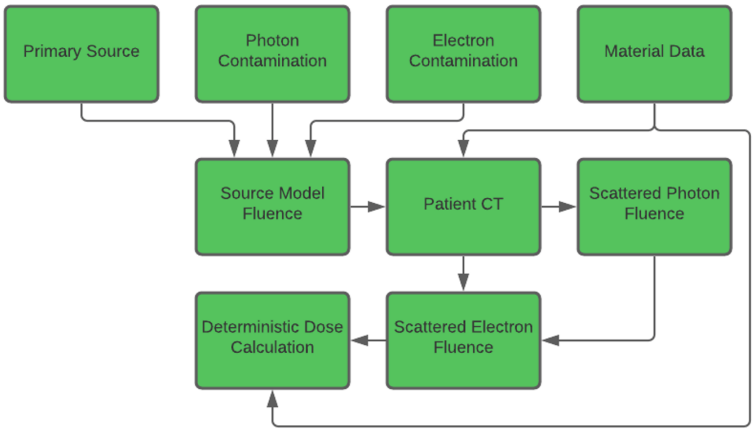

Figure 1.4: **General workflow of an LBTE algorithm. Interaction cross section and density data is used to directly model different tissues and radiation transport through the patient anatomy.**

entire treatment volume, the latter of which can be used to compute the dose within the volume.

Mathematical Formalism

For a region defined by volume V and surface δV, the LBTE is described by the following set of equations:

$$\hat{\Omega} \cdot \vec{\nabla}\Phi^{\gamma}(\vec{r}, E, \hat{\Omega}) + \sigma_t^{\gamma}(\vec{r}, E)\Phi^{\gamma}(\vec{r}, E, \hat{\Omega}) = q^{\gamma\gamma} + q^{\gamma} \tag{1.9}$$

$$\hat{\Omega} \cdot \vec{\nabla}\Phi^{e}(\vec{r}, E, \hat{\Omega}) + \sigma_t^{e}(\vec{r}, E)\Phi^{e}(\vec{r}, E, \hat{\Omega}) - \frac{\partial}{\partial E}[S_R(\vec{r}, E)\Phi^{e}(\vec{r}, E, \hat{\Omega})] = q^{ee} + q^{\gamma e} + q^{e} \tag{1.10}$$

where Eq. 1.9 represents the photon transport and Eq. 1.10 represents the electron transport. In Eq.'s 1.9 and 1.10, $\Phi^{\gamma}(\vec{r}, E, \hat{\Omega})$ is the photon angular fluence, $\Phi^{e}(\vec{r}, E, \hat{\Omega})$ is the electron angular fluence, $\sigma_t^{\gamma}(\vec{r}, E)$ is the macroscopic photon total cross section, $\sigma_t^{e}(\vec{r}, E)$ is the macroscopic electron total cross section, $S_R(\vec{r}, E)$ is the restricted collisional plus the radiative stopping power, $\vec{r} = (x, y, z) \in V$ is the spatial position vector, $E > 0$ is the energy, and $\hat{\Omega} = (\mu, \eta, \xi) \in 4\pi$ is a unit direction vector. The first term on the left-hand side of Eq.'s 1.9 and 1.10 represents how the particle fluence is changing in the direction of propagation, hence accounting for particle directionality. The second term on the left-hand side represents collisions by which particles are lost or created, namely scattering/production interactions. The third term on the left-hand side of Eq. 1.10 is the continuously slowing down operator, which accounts for particles lost by dissipating their

energy. The LBTE is subject to the boundary conditions of the system, most commonly the vacuum boundary condition given by

$$\Phi^{\gamma} = 0 \quad \text{for} \quad \hat{\Omega} \cdot \vec{n} < 0$$

$$\Phi^{e} = 0 \quad \text{for} \quad \hat{\Omega} \cdot \vec{n} < 0$$

where $\vec{n}$ is the outward directed unit normal vector to the surface δV. The right-hand side of Eq.'s 1.9 and 1.10 represent the scattering, production, and extraneous (primary and contamination) source terms. The photon source term due to photon interactions, $q^{\gamma\gamma}(\vec{r}, E, \hat{\Omega})$, is given by

$$q^{\gamma\gamma}(\vec{r}, E, \hat{\Omega}) = \int_0^{\infty} dE' \int_{4\pi} d\hat{\Omega}' \sigma_s^{\gamma\gamma}(\vec{r}, E' \rightarrow E, \hat{\Omega} \cdot \hat{\Omega}') \Phi^{\gamma}(\vec{r}, E', \hat{\Omega}') \tag{1.11}$$

The electron source term from photon interactions, $q^{\gamma e}(\vec{r}, E, \hat{\Omega})$, is

$$q^{\gamma e}(\vec{r}, E, \hat{\Omega}) = \int_0^{\infty} dE' \int_{4\pi} d\hat{\Omega}' \sigma_s^{\gamma e}(\vec{r}, E' \rightarrow E, \hat{\Omega} \cdot \hat{\Omega}') \Phi^{\gamma}(\vec{r}, E', \hat{\Omega}') \tag{1.12}$$

The electron source from electron interactions, $q^{ee}(\vec{r}, E, \hat{\Omega})$, is

$$q^{ee}(\vec{r}, E, \hat{\Omega}) = \int_0^{\infty} dE' \int_{4\pi} d\hat{\Omega}' \sigma_s^{ee}(\vec{r}, E' \rightarrow E, \hat{\Omega} \cdot \hat{\Omega}') \Phi^{e}(\vec{r}, E', \hat{\Omega}') \tag{1.13}$$

In Eq.'s 1.11, 1.12, and 1.13, $\sigma_s^{\gamma\gamma}$, $\sigma_s^{\gamma e}$, and σ_s^{ee} represent the macroscopic photon-to-photon differential scattering, photon-to-electron differential production, and electron-to-electron differential scattering cross sections, respectively. Physically, the photon-to-photon differential scattering cross section represents photons created from Compton scattering events while the photon-to-electron differential production cross section represents electrons created during photoelectric interactions, Compton interactions, and pair production (note that this model assumes both particles created during pair production are electrons, not one electron and one positron). The electron-to-electron differential scattering cross section represents ionization and excitation interactions between secondary electrons and electrons in the interaction volume. In reality, there should also exist an electron-to-photon term accounting for bremsstrahlung and annihilation radiation produced in the medium, but this model assumes that electrons do not produce photons and that the energy normally given to bremsstrahlung production is deposited locally. This is also evident in Eq. 1.10 since the S_R term accounts for restricted collisional and radiative stopping power. In practice, these

differential scattering cross sections can be simplified by expanding them in terms of Legendre polynomials. In addition, the angular fluence (both for photons and electrons) can be expanded in terms of spherical harmonics and spherical harmonic moments.

Dose Calculation

By nature, the LBTE is continuous. As analytical solutions only exist for a few simplified problems, solving the LBTE involves discretizing the LBTE in terms of its spatial, angular, and energy variables and using a computational approach to estimate its solution. By numerically solving for the angular electron fluence after discretization, the dose in a region i can be calculated using the following equation:

$$D_i = \int_0^\infty dE \int_{4\pi} d\hat{\Omega} \frac{\sigma^e_{ED}(\vec{r}, E)}{\rho} \Phi^e(\vec{r}, E, \hat{\Omega}) \tag{1.14}$$

where σ^e_{ED} is the macroscopic energy deposition cross section in units of MeV/cm and ρ is the density of the medium, leaving us with units of radiation dose. Note that the final dose calculation only involves electron cross sections, since electrons are the only particles that deposit their energy (and hence dose) in the medium. An advantage of using this approach is that the electron energy fluence is calculated everywhere in the region of interest. Therefore, to get the dose in the region of interest, one only needs to use Eq. 1.14 once the electron energy fluence is solved for. This makes it relatively simple to calculate dose-to-medium or dose-to-water by using the respective cross section and density data.

Heterogeneity Correction

Since solving the LBTE consists of directly solving for the photon and electron transport based on the medium of interest, heterogeneity is inherently modelled in the computation. Therefore, no heterogeneity correction is necessary. Solving the LBTE relies on the elemental composition of the medium in addition to the material density because the interaction cross sections are dependent on the chemical composition of the interaction medium. To get the dose to the medium, the Hounsfield unit is is taken from the CT scan and a look-up table is used to assign that Hounsfield unit to a certain

material with given cross section and density data. If the dose is calculated to water, water cross section data is used but the density of water is scaled according to the Hounsfield unit.

1.1.4 Monte Carlo Dose Calculation

Rather than the deterministic approach employed in Section 1.1.3, Monte Carlo dose calculation algorithms use a stochastic approach to solving the LBTE. The same math outlined in Section 1.1.3 applies to Monte Carlo, but rather than discretizing the LBTE and solving numerically Monte Carlo simulates the transport of a large number of particles through the medium through repeated random sampling of the probability density functions (PDF) derived from the interaction cross sections. The general workflow for a Monte Carlo dose calculation is shown in Fig. 1.5. Note that the workflow is the same as that shown in Fig. 1.4, but we now have a *stochastic* dose calculation compared to the deterministic approach of a gridded LBTE solver. The implementation of Monte Carlo dose calculation is beyond the scope of this work, but the reader is referred to a report by Liang and colleagues for further details on the implementation of Monte Carlo [12].

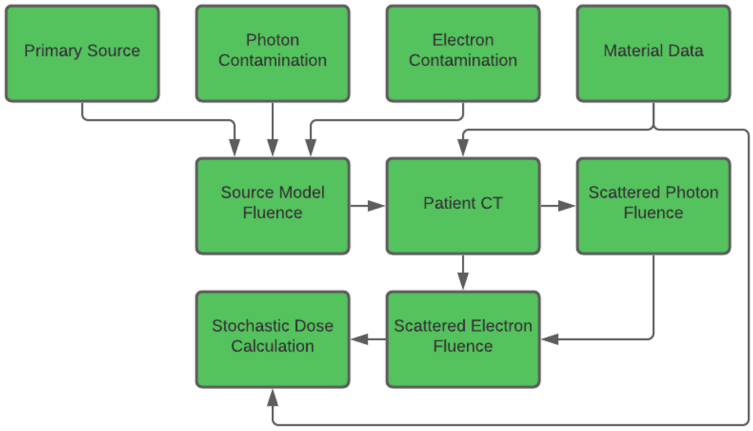

Figure 1.5: **Workflow for a Monte Carlo dose calculation. Radiation transport is simulated through random sampling of probability distributions representing different particle interactions.**

General Idea

The fundamental interaction cross sections calculated through the application of the Schrödinger equation to radiation transport are, by nature, probabilistic. Since the interaction cross sections are what determines how a particle interacts in the medium, repeated random sampling of cross section PDFs simulates how a particle beam interacts within a pateint geometry defined by a CT dataset. Tracing the energy deposition pattern of an interaction chain (also known as a "history") will give an accurate depiction of the dose distribution within the medium since the mass of material may be estimated from the CT dataset. Materials can be assigned to the CT dataset in a similar manner as the gridded LBTE solver, by which a certain range of Hounsfield units correspond to a given material with given density. For example, if a primary photon enters the patient and undergoes Compton scattering, the scatter photon will be tracked as well as the electron created through the Compton interaction. The electron will go on to deposit its energy near the interaction site (and hence give dose) and the scattered photon will go interact elsewhere. Deposited energy will begin to be accumulated in each voxel, which can then me normalized by the voxel mass to calculate the absorbed dose. Monte Carlo is able to account for all possible photon/electron interaction types, but interactions contributing negliglible dose may be omitted to speed up calculations. Since they solve the same fundamental problem, gridded LBTE solvers and Monte Carlo simulations will converge to the same solution if the LBTE solver is discretized in to infinitely small grids and if the Monte Carlo algorithm simulates an infinite number of particles. However, both of these are technologically infeasible, creating a tradeoff between calculation time and accuracy. In addition, clinical MV beams consist of millions of photons so a high number of particle histories must be tracked in order to minimize statistical uncertainty.

Heterogeneity Correction

Since the statistical simulation of radiation transport involves quantum-mechanical cross-sections, heterogeneity is inherently modeled in the algorithm, negating the need for any heterogeneity correction. The chemical composition and density of each material is explicitly modelled in a Monte Carlo calculation. Material data tables are used to define these elemental compositions

depending on the CT data provided. By altering the cross section and density data, Monte Carlo is able to report dose in terms of dose-to-medium or dose-to-water.

1.1.5 A Summarizing Exercise

The three types of algorithms fundamentally differ in the way they handle the problem of dose calculation. Advancements in computational power have allowed for the creation of more sophisticated dose calculation algorithms. Generally, type A algorithms refer to those employing a 2-D integration technique and handle heterogeneity by computing an equivalent path length along the beam propagation direction. Lateral heterogeneity is not accounted for as surrounding voxels are assumed to be water. Type B algorithms refer to those using a 3-D convolution technique by applying dose kernels to the fluence distribution within the patient anatomy. Heterogeneity corrections are employed along the beam path and laterally according to local electron density variations. This is not a rigorous model of heterogeneity, but rather a coarse approximation. The accuracy of the heterogeneity correction is very limited in a type B calculation. In addition, the medium is assumed to be water, so the chemical composition of the patient anatomy is not accounted for. Type C algorithms are those that rigorously model the physics of dose absorption and consider the chemical makeup of the patient anatomy. These algorithms employ a deterministic or stochastic approach to calculate dose and handle heterogeneity through material specification. A summary of the different algorithms and how they handle different aspects of dose calculation is shown in Table 1.1.

1.2 Dose Calculation in Lung Stereotactic Body Radiation Therapy

1.2.1 Management of Non-Small Cell Lung Cancer

Lung cancer remains a common cancer diagnosis for people in the United States. It is estimated that 235,760 people will be diagnosed with lung cancer this year alone in the United States [13]. One type of lung cancer, non-small cell lung cancer (NSCLC), accounts for roughly 85% of all

Table 1.1: **Summary table of how each type of algorithm handles the various aspects of dose calculation.**

Algorithm Type	Charged Particle Contamination	Photon Contamination	Longitudinal Heterogeneity	Lateral Heterogeneity	Elemental Composition	Computation Time
Type A	Exponential kernel with depth	Exponential kernel outside of primary beam	Equivalent path length along beam direction	No lateral correction	Assumed to be water	Fast
Type B	Monte Carlo derived kernel	Monte Carlo derived kernel	Equivalent path length along beam direction	Electron density-based scaling in lateral direction	Assumed to be water	Medium
Type C: Discrete LBTE solvers	Monte Carlo modelling of transport through treatment head	Monte Carlo modelling of transport through treatment head	Heterogeneity directly modelled	Heterogeneity directly modelled	Assigned to biological tissues depending on structure HU	Medium
Type C: Monte Carlo	Simulation through treatment head	Simulation through treatment head	Heterogeneity directly modelled	Heterogeneity directly modelled	Assigned to biological tissues depending on structure HU	Slow

lung cancer diagnoses [14]. The primary treatment for NSCLC depends mostly on cancer staging, with staging often performed using the TNM system [15] using a variety of diagnostic tools, such as medical imaging studies, lab work, and physical examinations. Surgical resection of the lesion is recommended if the patient is a surgical candidate [16]. Surgical procedures used in the treatment of NSCLC include pneumonectomy, sleeve resection, lobectomy, or limited resection [16, 17, 18]. Depending on post-operative pathological staging, adjuvant chemotherapy and/or radiation may be given.

Patients deemed medically inoperable or those who refuse surgery often undergo stereotactic body radiation therapy (SBRT) as their primary treatment method [17]. SBRT is a highly hypofractionated treatment regimen characterized by delivering a high amount of radiation dose over a small number of fractions (e.g. 18 Gy $\times$ 3 fractions to a total dose of 54 Gy) using highly conformal techniques. Due to the high dose per fraction in SBRT, accurate target localization and optimal margins are essential in reducing normal tissue toxicities while keeping tumor control high. Treatment outcomes in SBRT for early-stage NSCLC have been shown to be comparable to conventional surgery [19, 20, 21]. SBRT has proven to be an effective alternative treatment for early-stage NSCLC, but radiation dose calculation in lung SBRT can often be difficult and unreliable.

1.2.2 Dose Calculation Accuracy in Lung SBRT

Dose calculation in lung SBRT is complex due to the small fields utilized during treatment and the low density associated with lung tissue. Tumors situated in the low density lung parenchyma create great density heterogeneity within the treatment fields and produce a lung-tumor interface, both of which add further complexity for dose calculation. Modelling the electronic disequilibrium in situations like lung SBRT is difficult for most clinical dose calculation algorithms. Low density and small fields exacerbate electronic disequilibrium, making dose calculation difficult for lung SBRT cases. The dose calculation algorithms summarized above all handle heterogeneity differently, and hence result in different calculated dose distributions in lung SBRT.

Several studies have been performed comparing the dose distributions calculated with the different algorithms, and measurements have been made to investigate the accuracy of each algorithm. These studies have been done in phantoms and in clinical patient treatment plans. In homogeneous water phantoms, the differences between the algorithms are often small and can be neglected in most cases [22, 23, 24, 25]. This result is expected as the dose kernels employed in the pencil beam and convolution-superposition models are most often developed in homogeneous water phantoms. When heterogeneity is introduced in to the problem (either in the form of material slabs or patient anatomy), the algorithms begin to diverge from one another due to differences in how the algorithms handle heterogeneity. In particular, type A algorithms have been shown to overestimate the dose delivered in low density regions [22, 23, 24, 25, 26, 27, 28, 29, 30, 31]. One reason as to why the dose is overestimated is due to the penumbra widening observed in low density regions. Secondary electrons travel further in low density areas, leading to a wider penumbra and less dose being deposited near the interaction site. Since penumbra widening is not modelled in type A algorithms, the calculated dose will be higher than the actual delivered dose. Although more accurate than type A algorithms, type B algorithms can still differ from Monte Carlo simulations and measurements when tested in heterogeneous phantoms and patient treatment plans [22, 28, 29, 30, 32, 33, 34, 35, 36, 37, 38, 39, 40]. Kernel scaling in a limited number of directions is one reason for this discrepancy, as well as approximations made to determine the exact TERMA distribution within the patient and inaccurate modelling of the accelerator treatment head. Type

C dose calculation consistently shows the best agreement with measurements and is preferred for treatments affected by heterogeneity, as has been shown in previously cited work. However, discrepancies still exist between measurement and type C calculations. These mainly have to do with computational limitations, uncertainties in interaction data, and uncertainties in the problem being analyzed. Dose can only be calculated in discrete voxels, so dose can really only be sampled for small volumes dictated by the voxel size. This inevitably leads to partial volume averaging as a small volume of the patient represented by a voxel is treated as a point dose. However, advancements in computing power have made more robust computations possible and reasonably accurate. Only recently has type C dose calculation been implemented for clinical treatment planning and treatment validation.

The purpose of the following work is to explore the effects type C dose calculation may have on the dose distributions in lung SBRT treatment plans and to figure out how to best implement these new algorithms for clinical lung SBRT treatment planning. In addition, the effects of dosimetric accuracy on local control in lung SBRT will be explored.

Chapter 2

Implementation of LBTE Dose Calculation for Lung SBRT Planning

2.1 Introduction

The dose distributions calculated for lung SBRT plans using type B and type C algorithms can look very different. Typical prescription doses used in lung SBRT were developed based on comprehensive clinical trials [41, 42] which employed convolution-superposition dose calculation algorithms (type B) with heterogeneity corrections for treatment planning. In addition, physicians have developed their clinical experience using these algorithms, which poses a problem when looking to switch to type C dose calulation for lung SBRT treatment planning.

There is some guidance regarding the effect on clinical lung SBRT planning when switching from type A to type B dose calculation [43]. This study [43] shows how normalizing the plan dose based on planning target volume (PTV) coverage may not be appropriate when switching to type B dose calculation due to the large differences in dose between the two algorithms. In cases like these, coverage of the PTV periphery would be compromised due to the re-buildup region observed when transitioning from low to higher density regions. In addition, penumbra widening carries dose away from the target. To overcome this, the study recommended optimizing the fluence based on type A dose calculation, but use a type B algorithm when calculating the final dose and normalizing to the gross tumor volume (GTV) median dose. The study concluded this would be the best way to keep consistent lung SBRT outcomes.

A few studies have been done showing how lung SBRT workflows may be altered by switching to more advanced dose calcualtion algorithms [44, 45, 46, 47, 48]. Most of the studies focus on compliance with the Radiation Therapy Oncology Group (RTOG) 0813 and 0915 [41, 42] dosi-

metric criteria for central and peripheral non-small cell lung cancer. The criteria defined in the RTOG protocols were developed based on convolution-superposition algorithms employing heterogeneity corrections. The studies show when the lung SBRT treatment plans were recalculated with type C algorithms, more plans do not meet the dosimetric criteria specified by the protocols. This means switching to more advanced algorithms may substantially impact the dose distribution in lung SBRT and may necessitate a modification in the way insititutions develop their treatment plans. Switching to type C dose calculation had an effect on target dose parameters as well as organ at risk (OAR) parameters. PTV coverage was typically reduced upon recalculation with type C algorithms, but restoring PTV coverage through normalization resulted in worse RTOG compliance. However, the studies did not find any reason to modify the OAR dosimetric criteria defined in the protocol, specifically for the lung V20Gy, spinal cord maximum dose, heart D15cc, and esophagus D5cc.

While previous studies have extensively evaluated RTOG compliance using type C dose calculation algorithms, little guidance exists for clinics attempting to transition from type B dose calculation to type C dose calculation for lung SBRT planning. Specifically, no studies have evaluated how different normalization strategies change target and OAR dose or how they affect overall monitor units (MU). The purpose of this work is to evaluate the effect of different dose normalization strategies on target and OAR doses when shifting to type C dose calculation for lung SBRT.

2.2 Methods

2.2.1 Patient Cohort

85 lung SBRT patients treated from 2007-2014 at the Duke University Medical Center were selected from an institutional review board (IRB)-approved retrospective study protocol comparing SBRT and surgery for the treatment of Stage I NSCLC (Pro00106524). 87 total tumors were treated, all of which were classified as Stage I NSCLC with varying histology and location. A variety of PTV volumes were observed, ranging from 5.8-145.2 cc. Patients were prescribed 40-60 Gy in 3-8 fractions using 3-dimensional conformal radiation therapy (3DCRT) or intensity modulated

radiation therapy (IMRT) and treated on a Clinac 21EX, Novalis TX, TrueBeam, or TrueBeam STX (Varian Medical Systems, Palo Alto, CA, USA). At CT simulation, patients received 4-dimensional CT (4DCT), free-breathing CT, breath-hold CT, or a combination of the three depending on the motion management technique employed during treatment. Motion management techniques included free-breathing (FB), breath-hold (BH), or respiratory gating.

2.2.2 Target Volume Definition

Target volumes were defined differently for each patient depending on the motion management technique employed during treatment. ITV definition is dependent upon the respiratory management technique since the ITV accounts for tumor motion during a patient's breathing cycle. For patients treated with a FB technique ($n = 82$), the internal target volume (ITV) was defined as the union of the GTV contoured on the FB scan and the GTV contoured on the maximum intensity projection (MIP) of the 4DCT. For tumors treated with a gating technique ($n = 1$), the ITV was defined as the union of the contoured GTVs on each of the selected gating phases. For tumors treated with a BH technique ($n = 4$), the ITV was defined as the GTV contoured on the BH scan. PTVs were most often generated by a uniform expansion of the ITV with margin expansions ranging from 3-10 mm, most commonly 5 mm circumferentially ($n = 58$). If the expansion was not isotropic ($n = 2$), 8 mm was added in the superior-inferior directions with a 5 mm radial expansion. Variations in margin expansions were a result of differing tumor location and motion extent between patients.

2.2.3 Dose Calculation and Renormalization

The original treatment plans were calculated with AAA (versions 8.117, 8.223, 8.615, 10.028, and 11.031), which was the dose calculation algorithm commissioned at the time of treatment. After each version upgrade, dosimetric constancy tests were performed to verify dose calculation constancy. Patients enrolled in the IRB study whose doses were originally calculated with the Pencil Beam Convolution (PBC) algorithm were excluded from this work. The perecentage of the PTV covered by the prescription dose ranged from 80-100% with the large majority having $\geq$95% of the PTV covered by the prescription dose, as outlined in Table 2.1. Sufficient PTV coverage

Table 2.1: **Distribution of plan information.**

	Radiation Technique		Original PTV Coverage		
Beam Energy	**3DCRT**	**IMRT**	**100% covers 80-94%**	**100% covers 95%**	**100% covers 96-100%**
6X ($n = 54$)	46	8	4	26	24
10X ($n = 10$)	8	2	0	7	3
15X ($n = 6$)	6	0	0	2	4
Mixed ($n = 17$)	15	2	0	8	9
Total ($n = 87$)	**75**	**12**	**4**	**43**	**40**

Abbreviations: 3DCRT = 3-dimensional conformal radiation therapy; IMRT = intensity modulated radiation therapy; PTV = planning target volume.

was achieved by using volume-based normalization ($n = 81$), manual dose scaling ($n = 3$), or by defining a dose normalization point ($n = 3$). Each plan was recalculated with the recently commissioned AXB algorithm (version 15.603, reported as dose-to-medium, labelled AXBm) with fixed MU and leaving the plan geometry and relative beam weights unchanged. The rationale for reporting dose-to-medium follows from various studies and recommendations [32, 49, 50, 51]. The beam data used to commission AAA and AXB were the same, meaning any calculation differences between the two were not expected to be due to inconsistencies in beam data. For IMRT plans, the multileaf collimator (MLC) leaf sequence calculated in the AAA plan was copied over to the AXBm plan to keep a consistent MLC motion between plans. Once the plans were recalculated with AXBm, the AXBm were renormalized in three different ways:

1. Renormalized to cover 95% of the PTV with the prescription dose (PTV D95%[%] = 100%)
2. Renormalized to cover 99% of the ITV with the prescription dose (ITV D99%[%] = 100%)
3. Renormalized to match the original PTV coverage

2.2.4 Change in Delivered Dose

Percentage changes in total MU between the original AAA and the renormalized AXBm plans were calculated to investigate how the delivered dose (as quantified by total MU) may change when AXBm is implemented for lung SBRT planning. Since the original AAA plans were first recalculated with AXBm using fixed MU, a positive percentage change in total MU represents a delivered dose increase when renormalizing the AXBm plan.

2.2.5 Change in Treatment Planning System Reported Dose

Target Dose

To investigate how the treatment planning system (TPS) reported dose changes when implementing AXBm, the following dose statistics were collected for the PTV and ITV from the AAA and AXBm renormalized plans: D99%[Gy], Mean[Gy], and D1%[Gy]. Percentage differences were calculated between the AAA and renormalized AXBm dose metrics to quantify how the TPS reported dose changes when implementing AXBm. A positive value represents a reported dose increase relative to the AAA plan. For 10 randomly selected cases, a margin structure was created by subtracting the ITV from the PTV using a boolean operation. The change in mean dose from the AAA plan to the fixed MU AXBm plan was calculated for the margin strucutre and compared to the change in mean dose for the ITV to explore the spatial variation of the dosimetric differences between AAA and AXBm.

OAR Dose

TPS reported dose metrics collected for OARs included: spinal cord Max[cGy], esophagus Max[cGy], brachial plexus Max[cGy], skin Max[cGy], chest wall V30Gy[cc], lung V20Gy[%], and heart Max[cGy]. For the OAR dose metrics, absolute differences were calculated between the AAA and renormalized AXBm plans to better represent the dosimetric impact for a wide range of original OAR doses. A positive value represents an OAR TPS reported dose increase from the AAA plan to the renormalized AXBm plan. Our current institutional planning objectives were used to evaluate the OAR doses for the AAA and AXBm plans. The current institutional planning objectives are listed in Table 2.2. The OAR planning objectives currently used were conservatively set in reference to several studies investigating normal tissue toxicity in lung SBRT primarily based on a 3-fraction SBRT regimen [52, 53, 54, 55, 56]. All SBRT treatments *regardless of fractionation scheme* are planned to meet these objectives. Prior to treatment, the treating physician will evaluate the planned OAR dose based on the fractionation schedule being employed. If OAR dose is deemed too hot, a more fractionated regimen is considered. Changes in OAR doses after renormalization

Table 2.2: **Current OAR planning objectives used for lung SBRT planning.**

Organ at Risk	Planning Objective
Spinal Cord	Max[cGy] < 1,800 cGy
Esophagus	Max[cGy] < 2,000 cGy
Brachial Plexus	Max[cGy] < 2,400 cGy
Skin	Max[cGy] < 2,400 cGy
Chest Wall	V30Gy[cc] < 30 cc
Lungs	V20Gy[%] < 10%
Heart	Max[cGy] < 3,000 cGy

were investigated as well as the ability of the renormalized AXBm plans to meet the planning objectives. For plans where the chest wall planning objective was met in the AAA plan but was not met in the renormalized AXBm plan, the AXBm plan was reoptimized according to the AXBm-calculated dose to investigate the potential for improving chest wall dose while keeping the plan quality similar to that of the AAA plan.

2.3 Results

2.3.1 Change in Delivered Dose

A wide range of percentage changes in total MU were observed when renormalizing the AXBm plans. Boxplots showing the distribution of total MU changes for the three renormalization methods are shown in Fig. 2.1. Renormalizing the AXBm plans to the PTV D95% and keeping the original planned PTV coverage typically results in a delivered dose increase (median MU increases of 4.2% and 5.1%, respectively) while renormalizing the AXBm plans to the ITV D99% kept a similar delivered dose to the AAA plans (median MU decrease of 1.1%). A large spread of total MU changes were observed for all renormalization strategies with maximum increases of 44%, 23%, and 44% when renormalizing the AXBm plans to the PTV D95%, ITV D99%, and original planned PTV coverage, respectively.

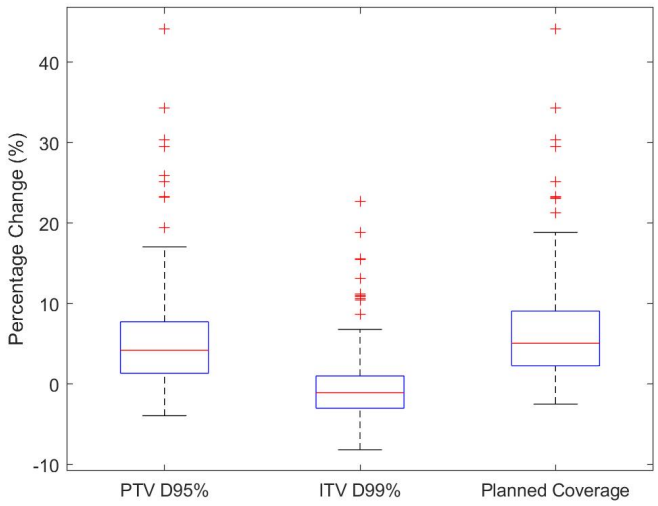

Figure 2.1: **Distribution of MU changes observed when renormalizing the AXBm plans. Data outliers are marked by the red plus signs.**

2.3.2 Change in Treatment Planning System Reported Dose

A variety of TPS reported dosimetric changes were observed when the AXBm plans were renormalized. Renormalizing the AXBm plans to the PTV D95% and original planned PTV coverage typically resulted in increased PTV, ITV, and OAR TPS reported doses while normalizing to the ITV D99% tended to result in decreased PTV, ITV, and OAR TPS reported doses. These findings are summarized in Tables 2.3 and 2.4. The largest median dose increases were observed in the PTV/ITV D1%[Gy] (3.4%/3.2% and 4.2%/4.0% when renormalizing the AXBm plans to the PTV D95% and original planned PTV coverage, respectively), esophagus Max[cGy] (22 and 26 cGy when renormalizing the AXBm plans to the PTV D95% and original planned PTV coverage, respectively), and the heart Max[cGy] (2.1 and 11 cGy when renormalizing the AXBm plans to the PTV D95% and original planned PTV coverage, respectively). The largest dose increases were observed in the spinal cord Max[cGy] (maximum increase of 467 and 606 cGy when renormalizing the AXBm plans to the PTV D95% and original planned PTV coverage, respectively), esophagus Max[cGy] (maximum increase of 705 cGy when renormalizing the AXBm plans to the PTV D95% and original planned PTV coverage), skin Max[cGy] (maximum increase of 675 cGy

Table 2.3: **Summary statistics for the percentage change in the PTV and ITV dose metrics when renormalizing the AXBm plans.**

Renormalization Method	Average (%)	Median (%)	Minimum (%)	Maximum (%)	(Q1*, Q3**) (%)
PTV D95%					
PTV D99%[Gy]	-2.2	-2.0	-6.4	2.5	(-3.3, -0.87)
ITV D99%[Gy]	2.5	1.8	-6.6	22	(0.41, 3.7)
PTV Mean[Gy]	3.5	2.4	-5.7	19	(0.64, 5.1)
ITV Mean[Gy]	5.2	3.4	-6.0	36	(0.89, 7.2)
PTV D1%[Gy]	6.4	3.4	-5.2	46	(1.4, 8.5)
ITV D1%[Gy]	6.4	3.2	-5.0	46	(1.1, 8.4)
ITV D99%					
PTV D99%[Gy]	-8.0	-7.6	-24	23	(-10, -5.2)
ITV D99%[Gy]	-3.8	-3.7	-8.5	-0.040	(-5.0, -2.6)
PTV Mean[Gy]	-2.9	-3.4	-9.3	6.5	(-4.9, -1.3)
ITV Mean[Gy]	-1.3	-2.4	-7.4	11	(-4.0, 0.0)
PTV D1%[Gy]	-0.22	-1.9	-7.3	19	(-3.7, 0.96)
ITV D1%[Gy]	-0.21	-1.9	-7.4	20	(-3.7, 0.92)
Planned Coverage					
PTV D99%[Gy]	-1.4	-0.88	-6.8	2.3	(-2.0, -0.20)
ITV D99%[Gy]	3.3	2.6	-2.3	22	(1.2, 4.7)
PTV Mean[Gy]	4.3	2.8	-1.9	19	(1.5, 6.0)
ITV Mean[Gy]	6.1	4.0	-2.7	36	(1.7, 8.2)
PTV D1%[Gy]	7.3	4.2	-0.87	46	(1.9, 9.4)
ITV D1%[Gy]	7.3	4.0	-1.9	46	(1.9, 9.6)

Abbreviations: PTV = planning target volume; ITV = internal target volume.
*First quartile
**Third quartile

Table 2.4: **Summary statistics for the absolute change in the OAR dose metrics when renormalizing the AXBm plans.**

Renormalization Method	Average	Median	Minimum	Maximum	(Q1*, Q3**)
PTV D95%					
Spinal Cord Max[cGy]	18	0.0088	-61	467	(-0.094, 0.23)
Esophagus Max[cGy]	53	22	-241	705	(-2.6, 68.3)
Brachial Plexus Max[cGy]	17	2.3	-102	126	(-2.6, 61)
Skin Max[cGy]	126	0.0080	-162	675	(-66, 281)
Chest Wall V30Gy[cc]	4.7	0.85	-3.9	40	(-0.11, 5.8)
Lung V20Gy[%]	0.27	0.15	-0.33	2.7	(0.020, 0.37)
Heart Max[cGy]	72	2.1	-90	1,554	(-14, 60)
ITV D99%					
Spinal Cord Max[cGy]	-29	-29	-162	297	(-67, -3.1)
Esophagus Max[cGy]	-19	-29	-296	362	(-58, 1.9)
Brachial Plexus Max[cGy]	-50	-22	-137	-5.0	(-89, -8.1)
Skin Max[cGy]	-33	-18	-353	424	(-189, 48)
Chest Wall V30Gy[cc]	-1.3	-1.8	-13	29	(-3.9, 0)
Lung V20Gy[%]	-0.15	-0.18	-0.87	1.5	(-0.34, -0.040)
Heart Max[cGy]	3.2	-12	-186	788	(-43, 4.7)
Planned Coverage					
Spinal Cord Max[cGy]	38	7.6	-78	606	(-11, 52)
Esophagus Max[cGy]	58	26	-151	705	(-0.38, 80)
Brachial Plexus Max[cGy]	38	2.3	-12	161	(-1.6, 61)
Skin Max[cGy]	127	0.0080	-162	675	(-66, 287)
Chest Wall V30Gy[cc]	5.3	1.7	-2.4	40	(0, 8.1)
Lung V20Gy[%]	0.32	0.18	-0.33	2.7	(0.070, 0.49)
Heart Max[cGy]	85	11	-53	1,554	(-7.9, 80)

Abbreviations: PTV = planning target volume; ITV = internal target volume.
*First quartile
**Third quartile

upon renormalizing the AXBm plans to the PTV D95% and original planned PTV coverage), and heart Max[cGy] (maximum increase of 1,554 cGy when renormalizing the AXBm plans to the PTV D95% and original planned PTV coverage). For the subset of patients in which a margin structure

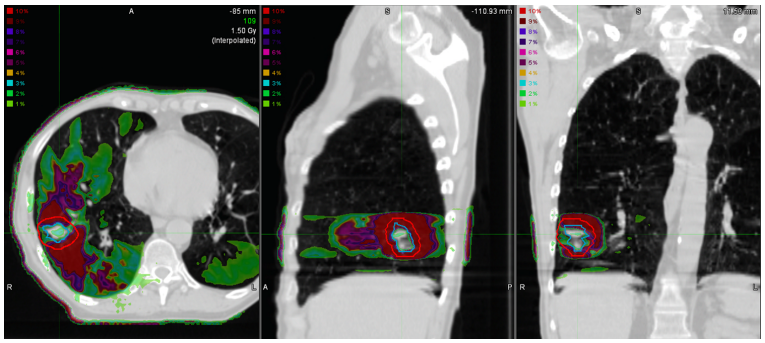

Figure 2.2: **Example dose difference map showing an increased dosimetric difference in the peripheral region of the PTV. Percentages are defined as the dose difference between AAA and AXBm normalized to the prescription dose.**

was generated, the change in the ITV mean dose was -1.8±2.1% compared to -4.4±4.5% for the margin structure. An example dose difference map for one of these plans is shown in Fig. 2.2.

2.3.3 OAR Planning Objective Compliance

Not all patients had every OAR contoured and not all plans met every objective listed in Table 2.2. To investigate how the implementation of AXBm may affect the ability to meet the institutional planning objectives, the number of instances where a given OAR objective was met in the original AAA plan but was not met in the renormalized AXBm plan were counted and are shown in Fig. 2.3. In some instances (such as with the chest wall), the method of renormalization had a substantial impact on the plan's ability to meet the institutional planning objectives. 10 patients whose original AAA plans met the chest wall objective did not meet the same objective in the AXBm plan when renormalizing to the PTV D95% or original planned PTV coverage compared to only 4 when normalizing to the ITV D99%. In all cases, renormalizing the AXBm plans to the ITV D99% resulted in a superior or equal ability to meet the OAR planning objectives compared to renormalizing to the PTV D95% or original planned PTV coverage.

For patients in which the chest wall objective was initially met in the AAA plan but not met when renormalizing the AXBm plan to the PTV D95% ($n = 10$), the AXBm plan was replanned. For 3DCRT plans, this was done by altering MLC aperture shapes, relative field weights, and/or beam energy. For IMRT plans, reoptimization was performed based on the AXBm-calculated dose.

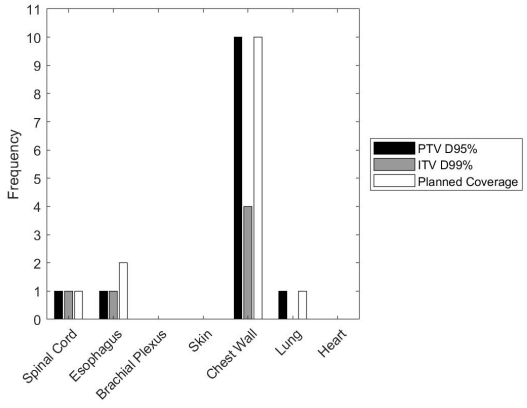

Figure 2.3: **Frequency of plans where the listed OAR planning objective was met in the original AAA plan but was not met in the renormalized AXBm plan, stratified by renormalization method.**

The chest wall V30Gy[cc] was recorded for each plan and are shown in Fig. 2.4. In every case, the replanned chest wall V30Gy[cc] met the planning objective and had little effect on other OAR doses. The TPS reported chest wall V30Gy[cc] decreased by a median 0.44 cc between the original AAA plan and the AXBm replan while the median decrease between the original AXBm PTV D95% plan and the AXBm PTV D95% replan was 10 cc.

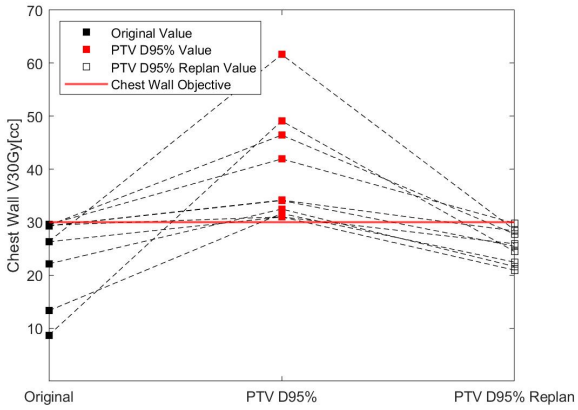

Figure 2.4: **Chest wall V30Gy[cc] progression from the original AAA plan, to the renormalized AXBm plan, to the replanned AXBm plan.**

2.4 Discussion

This study reports the experience of our clinic implementing the AXB algorithm for lung SBRT planning. The measurements and beam data acquired for the commissioning of the algorithms used in this study are unique to our institution. However, the increased dose heterogeneity observed when recalculating the AAA plans with AXB in this study is consistent with previous studies comparing type B and type C dose calculation in lung SBRT [25, 29, 30, 34, 36, 37, 38, 39, 48]. While this study heavily focuses on dose normalization when implementing AXB for lung SBRT planning, differences in the dose distributions calculated by AAA and AXB are apparent by the range of percentage changes in total MU when the AXB plans were renormalized. For the AXB plans, more MUs are often needed to maintain the same PTV coverage as plans calculated with AAA. Fewer studies have evaluated the effect on OAR dose when renormalizing plans calculated with type C algorithms in lung SBRT [34, 36, 37], but the results of this study are consistent with previous studies. The study by Calvo et al. reports discrepancies between type B and type C algorithms to be $8.13 \pm 24.3\%$ for the spinal cord maximum dose, which is very comparable to the range observed in our study. The study by Hardcastle et al. focused on the ipsilateral lung dose, with significant differences in the lung V20Gy observed between type B and type C algorithms. While this study focused on dose to the total lung volume, the lung V20Gy is likely to be confined to the ipsilateral lung, making the findings reported in our study consistent with this previous study. This apparent change in the dose distributions calculated with type C algorithms in lung SBRT may necessitate a change in the way plans are normalized and how normal tissue tolerances are developed.

An important distinction can be made between the delivered dose quantified by total MU and the TPS reported dose. The TPS reported dose is representative of the dose distribution calculated by the employed algorithm, taking in to account the geometry of the patient and the treatment itself. The total MU setting is representative of the amount of radiation being delivered to the patient. When recalculating a lung SBRT plan originally calcualted with AAA using AXB with fixed MU, the delivered radiation beams are the same but the apparent dose distribution changes because of differences in how the algorithms account for density heterogeneity and scatter disequilibrium. Normalizing the AXB plans to achieve some desired PTV coverage results in a change in the TPS

reported target and OAR metrics compared to the AAA calculations if said metrics are not corrupted by the way the dose is normalized (e.g., AAA and AXB plans normalized to the PTV D95% consequently will have the same PTV D95%[Gy]). However, the change in MU when renormalizing the plan better quantifies how the delivered radiation changes when implementing AXB for lung SBRT planning.

The anlaysis of the 10 patients in which margin structures were generated suggests the decreases observed in the PTV margin region are, on average, larger than in the ITV. While the sample size for this sub-analysis is relatively small, this result is expected since the periphery of the PTV primarily lies in the secondary build-up region. This result can be more or less pronounced depending on the size of the ITV, the PTV margin used, and the location of the PTV. In lung SBRT, larger PTV margins will consequently include more low-density lung tissue as a part of the PTV structure provided the expansion does not include other soft tissue structures (such as the mediastinum, chest wall, or liver). This makes adequately dosing the PTV periphery difficult and will introduce several stubborn voxels in to the PTV that may make the dose distirbution much more heterogeneous and make it more difficult to reach a desired PTV coverage. This effect is independent of the dose calcualtion algorithm, but it may have a substantial effect on the ability to normalize to a desired PTV coverage.

The clinical effects of implementing AXB for lung SBRT planning is not explored in this work. Restoring the TPS reported PTV coverage by normalizing the AXB dose to the PTV D95% or original planned PTV coverage would result in a delivered dose increase to targets and OARs as indicated by a total MU increase. While delivered dose increases may be desirable for local control, the effect of delivered dose increases on normal tissue toxicities has not been established. In addition, there exists extreme cases where normalizing for PTV coverage results in a delivered dose that is much higher than the AAA plan. This is evident by the outliers observed in Fig. 2.1. Nine of the outliers observed in Fig. 2.1 were outliers for each of the normalizations. The ITV D99% renormalization method introduced two additional outliers, presumably due to the smaller range of MU changes observed using this normalization method. In cases like these there are large differences between the dose distributions calcualted with AAA and AXB, and therefore normalizing

the AXB plans to achieve some desired PTV coverage may result in an impermissible high dose to normal tissue. Many factors can contribute to the magnitude of the dosimetric difference between AAA and AXB, including but not limited to lung volume, average PTV density, and beam energy. Larger lung volumes, lower PTV densities, and higher beam energy all enhance charged particled disequilibrium, causing the secondary build-up region in the lungs to have a larger effect on the dose distribution. 10 of the 11 total outliers observed in Fig. 2.1 had lung volumes exceeding the median lung volume of the cohort used in the study, and the one patient whose lung volume was less than the median was planned with 15X beam energy. All of the outliers from Fig. 2.1 had an average PTV CT value less than the median average PTV CT value of the cohort. The change in MU for the AXBm plans normalized to the PTV D95% versus the total lung volume and average PTV CT value is shown in Fig. 2.5. Despite large dose differences being present in some cases, if hotspots are kept within the ITV and doses to normal tissues are kept at acceptable levels, a normalization to the PTV may be appropriate. If the hotspot lies outside the ITV or if OAR doses are deemed too hot, a normalization to the ITV may be considered to keep similar dose levels to AAA. In some cases, the delivered dose quantified by total MU and the TPS reported dose may be lower when the AXB plan is normalized to the ITV, but whether or not this would influence the treatment outcome is unknown.

Renormalizing AXBm plans to the PTV D95% or keeping the original planned PTV coverage showed inferior ability to meet the institutional OAR planning objectives. However, there were very

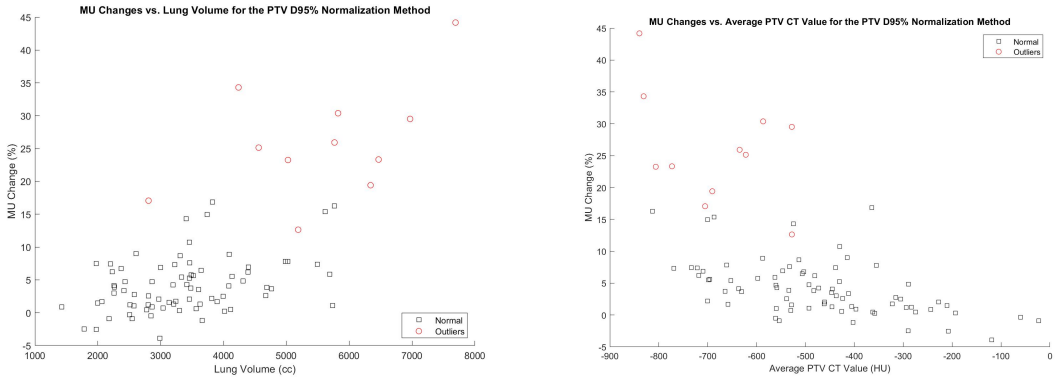

Figure 2.5: **Change in MU when renormalizing the AXBm plans to the PTV D95% versus total lung volume and the average PTV CT value.**

few cases for each OAR (besides the chest wall) where the associated planning objective was met in the original plan but was not met in the renormalized AXBm plan (see Fig. 2.3). The primary effect of the AXB algorithm is observed in the treatment region while OARs far from the treatment volume will be relatively unaffected by the implementation of the new algorithm. For the subset where the chest wall planning objective was met in the original AAA plan but not met in the AXBm plan renormalized to the PTV D95%, replanning of the AXBm PTV D95% plan showed how plan objectives not met after the initial renormalization are able to be met while maintaining the same PTV coverage and similar plan quality.

In this study, the maximum dose was used to evaluate the spinal cord, esophagus, brachial plexus, and heart doses. Issues may arise when using the maximum dose in comparison studies as the maximum dose metric is sensitive to the size of the structure of interest and the dose gradient surrounding said structure. We investigated the maximum dose for these structures to stay consistent with our institutional planning objectives. However, investigating the maximum dose should keep the same trends compared to other surrogates (such as D1% or D0.03cc, the "near maximum" dose), even though the data may be slightly noisier. In addition, it is important to note that some of the original AAA plans had less than 95% of the PTV covered by the prescription dose. In cases like these, normalizing the AXB plan to the PTV D95% will result in a delivered dose incresase even if the AXB calculation produced identical results to the AAA calculation. However, the number of cases where the original PTV coverage was less than 95% was small. These types of cases must carefully be assessed by the treatment planner and treating physician in order to keep doses to critical organs low while maintaining adequate PTV coverage.

2.5 Conclusions

More accurate dose calculation algorithms are beginning to be implemented for treatment planning, allowing for improved dosimetric accuracy in lung SBRT. The implementation of these new algorithms in to clinical practice may require a modification in how prescription doses are normalized and how institutional OAR planning objectives are developed due to differences in the

calculated dose distributions. Using AXB with the plan normalized for similar PTV coverage to AAA typically results in increased delivered dose to targets and OARs while normalizing to the ITV results in a delivered dose that is similar to AAA planning. For the AXB plans, the TPS reported dose increases when normalizing AXB plans to similar PTV coverage as AAA while TPS reported dose decreases when normalizing to the ITV. The OAR planning objectives are manageable with AXB planning while maintaining adequate PTV coverage. For extreme cases where normalizing the AXB plan for PTV coverage results in an unacceptable high dose, a plan normalization to the ITV may be considered to maintain similar dose levels to AAA planning.

Chapter 3

Retrospective Analaysis on the Effect of Dosimetric Accuracy on Treatment Outcome for SBRT/Hypofractionated Image-Guided Radiation Therapy for Early-Stage NSCLC

3.1 Introduction

The limited ability of type A and B dose calculation algorithms to model heterogeneity has raised issues regarding local control in lung SBRT. In some cases, the dose prescription appears to be fulfilled with type A or B algorithms, but when the plans are recalculated with type C algorithms the dose may be much lower. This dose overestimation when using type A or B algorithms has been shown in numerous studies [25, 48, 51, 57]. While some of the studies have shown the maximum target dose to increase, most of the studies show a decrease in other target dose metrics upon recalculation with type C algorithms. This means significant underdosing could potentially exist when clinically delivered lung SBRT plans are planned with type A or B algorithms.

Previous studies have evaluated the effect of using different dose calculation algorithms on local tumor control in lung SBRT [58, 59, 60, 61]. The retrospective studies by Latifi et al. [58] and Ohri et al. [60] showed an association between the dose calculation algorithm used and local control in SBRT for NSCLC. However, these studies compared type A algorithms to type B or C algorithms. The study by Song et al. [59] showed no significant differences in local control between groups planned with Monte Carlo and those planned with a ray tracing algorithm (type A [62]) when patients were treated with CyberKnife, although some of these patients were treated for metastatic disease. The matched-pair study by Zhuang et al. [61] showed no significant dose differences

between local failure and local control groups when their treatment plans were recalculated with a type C algorithm. There exists a relationship between the dose calculation algorithm used and local control in SBRT for early stage NSCLC, but no study to date has shown the magnitude of the dosimetric change upon recalculation with a type C algorithm to influence treatment outcome.

The purpose of this work is to quantify the dosimetric uncertainty associated with different dose calculation algorithms and to investigate their influence on local failure in SBRT for early-stage NSCLC. Specifically, we are testing if dosimetric uncertainties associated with different algorithms are correlated with local failure while accounting for relevant clinical variables.

3.2 Methods

3.2.1 Patient Cohort

162 patients previously treated with SBRT or hypofractionated image-guided radiation therapy (HIGRT) for early-stage NSCLC from 2006-2018 at the Duke University Medical Center were selected from a retrospective protocol approved by our IRB (Pro00106524). In total, 164 tumors were treated. Patients were treated on a Clinac EX, Novalis TX, TrueBeam, or TrueBeam STX linear accelerator (Varian Medical Systems, Palo Alto, CA, USA) with 3DCRT, IMRT, or volumetric modulated arc therapy (VMAT) to a prescribed dose of 36-60 Gy over 3-8 fractions. Regimens with the number of fractions exceeding 5 were considered HIGRT, most of which are used to treat ultra central tumors. A variety of prescription normalizations were used. At CT simulation, patients underwent 4DCT, FB CT, BH CT, or a combination of the three depending on the motion management technique used. Motion management techniques included FB, BH, or respiratory gating. Patient and plan information is given in Table 3.1.

3.2.2 Target Volume Definition

The employment of different motion management techniques produced an inconsistency in ITV definition across the patient cohort. For patients treated FB, the ITV was defined as the union of

Table 3.1: **Patient, plan, and tumor information, stratified by treatment outcome.**

Parameter	Total (n=162)	Local Failure? Yes (n=15)	Local Failure? No (n=147)
***Sex**			
Male	77 (47.5%)	6 (40%)	71 (48.3%)
Female	85 (52.5%)	9 (60%)	76 (51.7%)
****Patient Age at Treatment (yr)**	75 (68, 81)	75 (66, 79)	75 (69, 81)
****Follow-Up Time (mo)**	21.7 (9.1, 46.2)	29.1 (16.0, 56.8)	22.2 (9.3, 45.1)
Number of Lesions	164	15	149
****Tumor Size (cm)†**	2.2 (1.5, 2.9)	3.0 (2.1, 3.5)	2.1 (1.5, 2.8)
***Respiratory Management Technique**			
Free-Breathing	153 (93.3%)	15 (100%)	138 (92.6%)
Gating	4 (2.4%)	0 (0%)	4 (2.7%)
Breath-Hold	7 (4.3%)	0 (0%)	7 (4.7%)
***Radiation Technique**			
3DCRT	123 (75%)	8 (53.3%)	115 (77.2%)
IMRT	31 (18.9%)	5 (33.3%)	26 (17.4%)
VMAT	10 (6.1%)	2 (13.3%)	8 (5.4%)
***Tumor Location†**			
Central	31 (18.9%)	4 (26.7%)	27 (18.1%)
Peripheral	125 (76.2%)	11 (73.3%)	114 (76.5%)
***Beam Energy**			
6X	81 (49.4%)	9 (60%)	72 (48.3%)
10X	51 (31.1%)	4 (26.7%)	47 (31.5%)
15X	10 (6.1%)	0 (0%)	10 (6.7%)
Mixed Energies	22 (13.4%)	2 (13.3%)	20 (13.4%)
***Algorithm**			
AAA	156 (95.1%)	13 (86.7%)	143 (96%)
PBC	8 (4.9%)	2 (13.3%)	6 (4%)
***Clinical T-Stage**			
T1 (a, b, c)	128 (78%)	9 (60%)	119 (80%)
>T1 (T2a, T2b, T3)	32 (19.5%)	6 (40%)	26 (17.4%)

Abbreviations: 3DCRT = 3-dimensional conformal radiation therapy; IMRT = intensity modulated radiation therapy; VMAT = volumetric modulated arc therapy; AAA = Anisotropic Analytical Algorithm; PBC = Pencil Beam Convolution; Q1 = 1st quartile; Q3 = 3rd quartile.
*n (%)
**Median (Q1, Q3)
†Incomplete data

the GTV contoured on the FB CT scan and the contoured GTV on the MIP of the 4DCT data set. For patients treated with BH the ITV was defined as the GTV contoured on the BH CT scan. For treatments utilizing respiratory gating, the ITV was defined as the union of the contoured GTVs from each of the selected gating phases. An isotropic expansion of the ITV ranging from 3-10 mm was typically used to generate the planning target volume (PTV), most commonly 5 mm ($n = 104$). If the margin expansion was not isotropic, 5 mm was added radially and the superior/inferior expansion was variable depending on the extent of tumor motion and/or proximity to OARs.

3.2.3 Dose Calculations

The clinically delivered treatment plans, calculated in the Varian Eclipse TPS, had their doses calculated using the AAA ($n = 156$) (versions 8.117, 8.223, 8.615, 10.028, 11.031, or 13.623), or the PBC algorithm ($n = 8$) (versions 7.522, 8.03, 8.117, or 8.223) using varying dose grids (most commonly 2.5 mm isotropic or a left/right anterior/posterior size of 2.5 mm with superior/inferior resolution dictated by the CT slice thickness). Dosimetric accuracy was verified after each version

upgrade to verify calculation constancy from version to version as a part of the clinical quality assurance program. Each clinical plan was recalculated with AXB (version 15.603) using fixed MU and leaving the plan geometry and relative field weights unchanged. The AXB doses were reported as dose-to-medium (AXBm). For plans using IMRT or VMAT techniques, the MLC leaf sequence was copied to the recalculated plan to keep consistent MLC motions.

3.2.4 Dose-Volume Data

The following dose-volume metrics were collected from the original and recalculated plans for both the PTV and ITV: Mean[Gy], D99%[Gy], D95%[Gy], D1%[Gy], and V100%[%]. The mean lung dose and lung V12Gy[cc] were also recorded for each plan. Each PTV and ITV dose metric was used to calculate a biologically effective dose (BED), which allows direct comparison between different fractionation schedules. The equation used to calculated the BED is:

$$\text{BED} = nd\left(1 + \frac{d}{\alpha/\beta}\right) \tag{3.1}$$

where n is the number of fractions, d is the dose per fraction, and α/β is a parameter derived from the linear-quadratic (LQ) model of cell killing representing the inherent radiosensitivity of the tissue of interest (these values can be found in the literature). Physically, the BED represents the total dose needed to provide the same cell kill as the fractionation schedule being studied at an infinitely low dose rate [63]. Although some data suggests a higher value [64], NSCLC treated with SBRT is assumed to have an α/β of 10 Gy [65], which was the value used in the calcualtions. Tumor control probabilities (TCP) were calculated using a Bayesian logistic regression model developed by Klement et al. [64]. The equation used to calculate TCP is given below:

$$\text{TCP} = \frac{\exp(b_0 + b_{\text{BED}} \cdot \text{BED}_i(\alpha/\beta) + b_l \cdot l_i)}{1 + \exp(b_0 + b_{\text{BED}} \cdot \text{BED}_i(\alpha/\beta) + b_l \cdot l_i)} \tag{3.2}$$

where $\text{BED}_i(\alpha/\beta)$ is the BED derived from the average between the PTV D95% BED and the PTV D1% BED for tumor i, l_i is the size of tumor i in cm, and b_0, b_{BED}, and b_l are regression coefficients computed in the regression. The values of b_0, b_{BED}, and b_l were reported to be -2.474, 0.0348 Gy^{-1}, and -0.451 cm^{-1}, respectively. Tumor size was defined based on a measurement made on

the diagnostic CT study. This value was typically defined to be the largest diameter measured in the axial and coronal planes.

3.2.5 Verification of the AXBm Calculations

Based on the availability of beam models, a subset ($n = 89$) of the cohort had their treatment plans recalculated with Monte Carlo to verify the accuracy of the AXBm calculations. Beam model availability only allowed for comparison of AAA and AXBm to Monte Carlo. Monte Carlo dose calculations were performed using the clinical SciMoCa^{TM} software package (Scientific RT, Munich, Germany), which has previously been validated against the Monaco and Pinnacle treatment planning systems [66]. Dose was calculated in SciMoCa^{TM} (SMC) using both dose-to-water and dose-to-medium for comparisons to AAA and AXBm, respectively. Comparisons between AAA, AXBm, and SMC were carried out for the PTV Mean[Gy] and D95%[Gy] as well as for the mean lung dose and lung V12Gy[cc].

3.2.6 Dose Comparisons

Reporting Modes

PBC and AAA report dose as dose-to-water while AXB inherently calculates dose-to-medium. However, AXB doses can also be reported as dose-to-water through post-processing of the calculation results. To investigate the effects of different reporting methods, dose-to-water (labelled AXBw) calculations were performed for a subset of the patient cohort ($n = 93$). Comparisons of the dose-volume data for the AXBm and AXBw calculations were carried out to investigate the differences between the two reporting modes.

Algorithm Comparisons

The percentage change in all dose metrics mentioned in Section 3.2.4 were calculated between the original plans and the recalculated AXBm plans. Trends were identified through graphic

investigation and the acquisition of summary statistics. To quantify how different the dosimetric uncertainties may have been had the PBC cases been planned with AAA, all cases originally planned with PBC were recalculated with AAA (version 15.603) to investigate the dosimetric differences between PBC and AAA. Doses from PBC were plotted against doses from AAA to look for trends in the differences between the two algorithms and compare them relative to AXB.

3.2.7 Multivariable Regression

Dose differences for each metric were calculated between the clinical and AXBm plans, as well as for the subset calculated in SMC. A regression analysis using the general linear model with 6 response variables and 9 predictor variables was carried out in MATLAB (MathWorks, Natick, MA, USA) to analyze the effects of beam energy, radiation technique, PTV volume, lung volume, and the PTV density and variability (as defined by CT) on the extent of the dosimetric changes when recalculating plans with AXBm. Only plans originally calculated with AAA were included in the multivariable regression. The regression method forms a system of linear equations based on the chosen predictor and response variables and calculates the regression coefficients by obtaining a best-fit solution to the response variables. Regression coefficients were calculated using the maximum likelihood estimation method. For our response and predictor variables, the system of equations had the following form:

$$\begin{bmatrix} y_{1,1} & y_{1,2} & y_{1,3} & y_{1,4} & y_{1,5} & y_{1,6} \\ y_{2,1} & y_{2,2} & y_{2,3} & y_{2,4} & y_{2,5} & y_{2,6} \\ \vdots & \vdots & \vdots & \vdots & \vdots & \vdots \\ y_{n,1} & y_{n,2} & y_{n,3} & y_{n,4} & y_{n,5} & y_{n,6} \end{bmatrix} = \begin{bmatrix} 1 & x_{1,1} & x_{1,2} & \dots & x_{1,9} \\ 1 & x_{2,1} & x_{2,2} & \dots & x_{2,9} \\ \vdots & \vdots & \vdots & \ddots & \vdots \\ 1 & x_{n,1} & x_{n,2} & \dots & x_{n,9} \end{bmatrix} \begin{bmatrix} \beta_{0,1} & \beta_{0,2} & \beta_{0,3} & \beta_{0,4} & \beta_{0,5} & \beta_{0,6} \\ \beta_{1,1} & \beta_{1,2} & \beta_{1,3} & \beta_{1,4} & \beta_{1,5} & \beta_{1,6} \\ \vdots & \vdots & \vdots & \vdots & \vdots & \vdots \\ \beta_{9,1} & \beta_{9,2} & \beta_{9,3} & \beta_{9,4} & \beta_{9,5} & \beta_{9,6} \end{bmatrix} + \begin{bmatrix} \epsilon_{1,1} & \epsilon_{1,2} & \epsilon_{1,3} & \epsilon_{1,4} & \epsilon_{1,5} & \epsilon_{1,6} \\ \epsilon_{2,1} & \epsilon_{2,2} & \epsilon_{2,3} & \epsilon_{2,4} & \epsilon_{2,5} & \epsilon_{2,6} \\ \vdots & \vdots & \vdots & \vdots & \vdots & \vdots \\ \epsilon_{n,1} & \epsilon_{n,2} & \epsilon_{n,3} & \epsilon_{n,4} & \epsilon_{n,5} & \epsilon_{n,6} \end{bmatrix} \tag{3.3}$$

Here, $y_{n,i}$ is the percentage change in the ith dose metric for the nth treatment plan ($i \in [1,6] \cap \mathbb{Z}$, $n \in [1,164] \cap \mathbb{Z}$), $x_{n,j}$ is the value of the jth predictor for the nth treatment plan ($j \in [1,9] \cap \mathbb{Z}$), $\beta_{m,i}$ are the regression coefficients calculated in the model relating the intercept and jth predictor metric to the ith dosimetric change metric ($m \in [0,9] \cap \mathbb{N}$), and $\epsilon_{n,i}$ constitutes a noise matrix accounting for the statistical variability of the data set. Binary variables were used to represent beam energy and treatment technique due to the discrete nature of those variables. The reference set was defined to be plans using 6X energy with a 3DCRT technique.

3.2.8 Survival Analysis

Association of the dosimetric uncertainties with local failure was investigated using a variety of statistical analyses. Univariate analyses (UVA) were performed using Fine and Gray's sub-distribution hazards model to quantify the effect of the dosimetric decrease on the risk of local failure. The mathematical formalism of Fine and Gray's sub-distribution hazards analysis is beyond the scope of this work, but the reader is referred to the original work by Fine and Gray [67] for further information. Patients who died without failure were treated as a competing event while patients who were lost to follow-up were censored. Using the same method, several multivariate analyses (MVA) were performed. In the MVA, PTV volume, clinical T-stage, and/or tumor location were controlled for. PTV volume and tumor location were selected as controls because PTV volume is well-defined and is expected to be correlated with clinical T-stage (higher T-stages are correlated with higher risk [15]), while tumor location is a clinically relevant variable independent of the other two. Kaplan-Meier (KM) plots were generated to show the effect of the variables controlled for in the MVA on treatment outcome. The KM analysis censors patients who died without failure, so competing risks were not accounted for. Patients with no follow-up or whose follow-up did not exceed six months were excluded from UVA, MVA, and KM analysis.

3.3 Results

3.3.1 Verification of the AXBm Calculations

AXBm had better agreement with SMC than did AAA. The median difference in the PTV D95%[Gy] was -7.0% and -1.7% when comparing AAA to SMC and AXBm to SMC, respectively. Full results of this analysis are shown in Table 3.2. Given the results of this analysis and previous studies, it is reasonable to assume the AXBm calculations produce an acceptable surrogate for the actual dose distribution within the calculation volume.

Table 3.2: **Comparison of select dose volume statistics between the different dose calculation algorithms. AXBm was closer to SMC than AAA for all investigated dose metrics. Negative values indicate SMC to be lower.**

	Average Dose Difference	
Dose-Volume Metric	**AAA and MC**	**AXBm and MC**
PTV Mean Dose	-4.9±5.3%	-0.2±1.0%
PTV D95%[Gy]	-9.2±7.6%	-1.4±1.8%
Mean Lung Dose	-2.4±1.7%	-0.6±1.3%
Lung V12Gy[cc]	-1.8±5.1%	-1.0±1.6%

Abbreviations: AAA = Anisotropic Analytical Algorithm; MC = Monte Carlo; AXBm = Acuros XB, dose-to-medium; PTV = planning target volume.

3.3.2 Dosimetric Differences Between Reporting Modes and Algorithms

Dose-to-Medium vs. Dose-to-Water

The differences between AXBm and AXBw were very small. The average difference between the two reporting modes was -0.55±0.98 Gy and -0.84±1.15 Gy for the PTV and ITV mean BEDs, respectively, and -0.17±1.25 Gy and -0.86±1.11 Gy for the PTV and ITV D95% BEDs, respectively. A negative value indicates dose-to-water to be lower.

Differences Between Algorithms

The observed dosimetric differences between plans originally calculated with PBC and AXBm were, on average, larger than the differences observed between plans originally calculated with AAA and AXBm. The average differences between PBC and AXBm for the PTV D99%, mean, and D1% BEDs were -25.6±19.2%, -15.9±11.2%, and -4.8±8.4%, respectively, compared to -11.6±11.0%, -4.6±6.1%, and -0.1±2.6%, respectively, between AAA and AXBm. All of the PBC plans recalculated with AAA showed the AAA calculated dose to be lower, as is shown in Fig. 3.1.

3.3.3 Multivariable Regression

The results of the regression analysis are shown in Tables 3.3 and 3.4. The PTV and ITV D1% BEDs are expected to increase when using IMRT or VMAT techniques. The beam energy

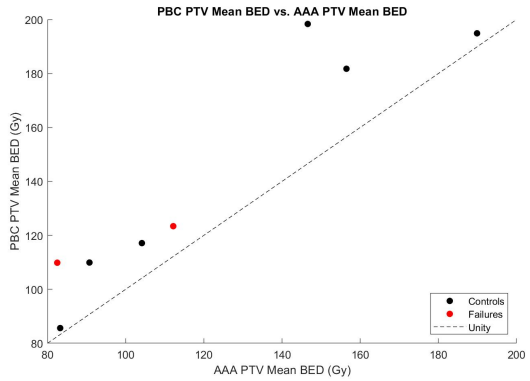

Figure 3.1: **PBC PTV Mean BED plotted against the AAA PTV Mean BED, showing PBC doses to be higher than the recalculated AAA doses. Similar plots can be made for the other dose metrics.**

Table 3.3: **Effect of beam energy and treatment technique on the dosimetric uncertainty of the selected dose metrics after the clinical plans were recalculated with AXBm. A negative value indicates a decrease in the metric upon recalculation with AXBm.**

	Expected change in:					
Parameter	**PTV D99% BED**	**ITV D99% BED**	**PTV Mean BED**	**ITV Mean BED**	**PTV D1% BED**	**ITV D1% BED**
6X (n=75)	-9.2%	-4.4%	-3.6%	-2.1%	-1.1%	-1.1%
10X (n=51)	-13.0%	-6.8%	-5.9%	-3.0%	-0.6%	-0.4%
15X (n=9)	-21.5%	-9.7%	-9.1%	-4.0%	-2.0%	-2.0%
Mixed (n=21)	-13.1%	-6.1%	-4.9%	-2.3%	-1.1%	-0.8%
IMRT (n=29)	-8.8%	-5.2%	-2.9%	-1.3%	2.1%	1.6%
VMAT (n=10)	-9.3%	-2.7%	-1.9%	-0.4%	2.8%	2.7%

Abbreviations: IMRT = intensity modulated radiation therapy; VMAT = volumetric modulated arc therapy; PTV = planning target volume; ITV = internal target volume, BED = biologically effective dose.

Table 3.4: **Effect of PTV size, lung volume, PTV density, and PTV density variability on the dosimetric uncertainty of the selected dose metrics after recalculation with AXBm. A negative value indicates a decrease upon recalculation with AXBm.**

	Expected change in:					
Variable Changed	**PTV D99% BED**	**ITV D99% BED**	**PTV Mean BED**	**ITV Mean BED**	**PTV D1% BED**	**ITV D1% BED**
PTV Volume (per 25 cc)	-0.2%	-0.2%	-0.2%	-0.2%	-0.2%	-0.2%
Lung Volume (per 500 cc)	-1.6%	-1.0%	-0.8%	-0.4%	-0.2%	-0.1%
Average PTV CT Value (per 100 HU)	3.1%	1.9%	1.4%	0.4%	-0.1%	-0.2%
Standard Deviation of PTV CT Value (per 50 HU)	-1.0%	0.1%	0.4%	0.4%	-0.2%	-0.3%

Abbreviations: PTV = planning target volume; CT = computed tomography; HU = Hounsfield unit; ITV = internal target volume; BED = biologically effective dose.

had a substantial impact on the magnitude of the dosimetric changes. The expected change in the PTV mean BED was -3.6%, -5.9%, and -9.1% for plans using 6X, 10X, and 15X, respectively. Increased lung volume was associated with increased dosimetric differences (expected decrease in PTV D99% BED of 1.6% per 500 cc). The PTV D99% and mean BEDs were expected to increase relative to AAA as the average PTV CT value increased (expected increase of 3.1% and 1.4%,

respectively). PTV volume did not have much of an influence on the magnitude of the dosimetric changes.

3.3.4 Survival Analysis

15 of the 162 patients experienced local failures (9.3%). For the tumors that locally recurred, the clinical and AXBm BED, V100%[%], and TCP distributions were, on average, lower compared to tumors that were controlled. Table 3.5 shows the median and interquartile ranges for each of the selected dose metrics, stratified by treatment outcome. A variety of changes were seen in all metrics upon recalculation with AXBm. Figure 3.2 shows the change in the PTV mean BED, ITV mean BED, and TCP upon recalculation with AXBm for each of the patients included in the failure analysis. Since the TCP should increase with an increased BED (see Equation 3.2), TCPs were plotted against the PTV and ITV mean BEDs. These plots are shown in Fig. 3.3,

Table 3.5: **Clinical and AXBm dose statistics, stratified by treatment outcome. * = Median (Q1, Q3). Q1 = 1st quartile, Q3 = third quartile.**

	Clinical Dose Stats		AXBm Dose Stats	
Parameter	**Failures**	**Controls**	**Failures**	**Controls**
PTV Mean BED* (Gy)	118.4 (109.9, 123.9)	120.4 (113.5, 166.6)	112.2 (107.0, 121.1)	117.6 (109.1, 158.1)
ITV Mean BED* (Gy)	119.7 (112.0, 133.0)	125.1 (118.2, 173.8)	116.0 (108.4, 127.8)	123.7 (115.2, 171.8)
PTV D95% BED* (Gy)	106.3 (100.1, 113.5)	112.5 (102.5, 151.2)	100.5 (95.9, 110.1)	104.6 (95.7, 131.6)
ITV D95% BED* (Gy)	115.1 (109.0, 126.3)	118.4 (111.7, 164.9)	113.0 (104.7, 121.0)	114.2 (108.4, 155.3)
PTV D1% BED* (Gy)	123.9 (115.6, 138.5)	131.7 (123.6, 182.2)	119.7 (115.1, 134.3)	131.3 (122.4, 183.5)
ITV D1% BED* (Gy)	124.4 (115.3, 139.2)	133.6 (124.1, 182.1)	119.8 (114.1, 135.3)	133.1 (121.9, 184.7)
PTV D99% BED* (Gy)	100.1 (96.6, 109.7)	108.7 (98.5, 145.4)	94.9 (86.0, 104.5)	97.6 (89.5, 123.0)
ITV D99% BED* (Gy)	113.0 (106.0, 121.7)	116.7 (109.3, 161.6)	111.4 (103.0, 115.4)	111.5 (103.9, 150.6)
PTV V100%[%]*	95 (95, 96)	95 (95, 97)	90 (74, 93)	82 (68, 91)
ITV V100%[%]*	100 (100, 100)	100 (100, 100)	100 (94, 100)	100 (96, 100)
TCP	0.55 (0.48, 0.67)	0.70 (0.58, 0.93)	0.51 (0.42, 0.62)	0.68 (0.56, 0.90)

Abbreviations: PTV = planning target volume; ITV = internal target volume; BED = biologically effective dose; TCP = tumor control Probability; AXBm = Acuros XB, dose-to-medium.

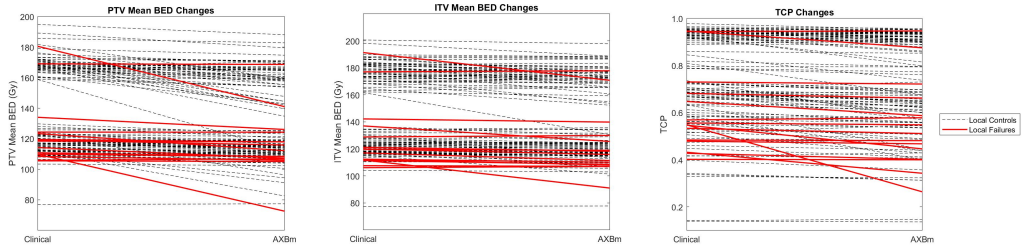

Figure 3.2: **Dosimetric change in the PTV/ITV mean BED and TCP when the original treatment plans were recalculated with AXBm. A negative slope indicates a decrease in BED upon recalculation.**

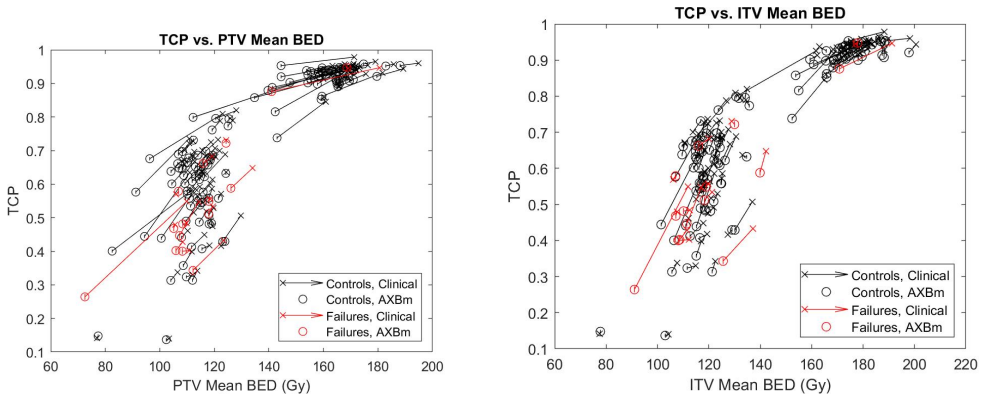

Figure 3.3: **TCP plotted against the PTV and ITV mean BEDs. Arrows are drawn from the clinical data points to the AXBm data points showing the magnitude of the dosimetric change upon recalculation with AXBm.**

which also show the magnitude of the dosimetric change upon recalculation with AXBm. A large range of dosimetric changes were seen in both patients who failed and those who were controlled. Boxplots were generated to investigate the spread of the dosimetric changes seen for all metrics upon recalculation with AXBm, stratified by treatment outcome. The boxplots are shown in Fig. 3.4.

126 patients fit the inclusion criteria for the UVA and MVA, 15 of which experienced local

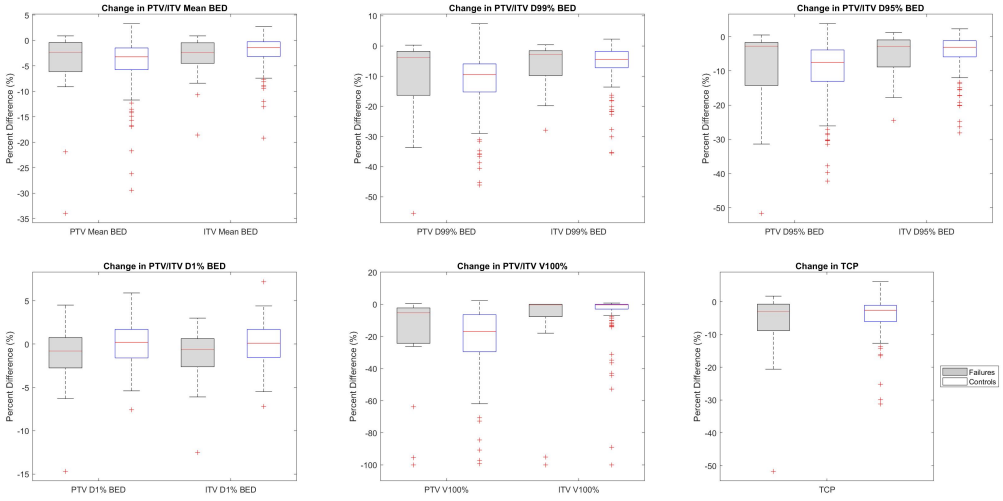

Figure 3.4: **The spread of the dosimetric changes seen for each of the metrics, stratified by treatment outcome. Negative values indicate a decrease in the metric upon recalculation with AXBm.**

Table 3.6: **Results of the UVA indicating the effect of the magnitude of the dosimetric change on the risk of local failure.**

Dose-Volume Metric	Hazard Ratio	95% Confidence Interval	p-value
PTV Mean BED	0.98	0.90-1.07	0.70
ITV Mean BED	0.93	0.85-1.03	0.16
PTV D95% BED	1.01	0.94-1.08	0.86
ITV D95% BED	0.99	0.92-1.06	0.73
PTV D1% BED	0.89	0.80-0.99	0.042
ITV D1% BED	0.87	0.78-0.98	0.023
PTV D99% BED	1.01	0.94-1.08	0.76
ITV D99% BED	0.99	0.93-1.06	0.84
PTV V100%	1.0	0.98-1.03	0.84
ITV V100%	0.99	0.98-1.0	0.14
TCP	0.97	0.93-1.0	0.067

Abbreviations: PTV = planning target volume; ITV = internal target volume; TCP = tumor control probability; BED = biologically effective dose.

failure, 10 of which experienced a competing event, and 101 of which were censored. The results of the UVA are shown in Table 3.6. Hazard ratios (HR) with $p<0.05$ were considered to be statistically significant. The results of the MVA are shown in Table 3.7. The significant parameters found in the UVA (see Table 3.6) were included in the MVA to control for the effect of various clinically relevant parameters. The PTV and ITV D99% BEDs were included because significant underdosing is expected to be associated with local failure.

KM plots showing the influence of relevant clinical parameters on local control for lung SBRT are shown in Fig. 3.5. Significant differences in local control were seen for patients with PTV volume greater than the median volume of the cohort and PTV volume less than the median, with a higher local control rate observed for patients with smaller PTV volumes. Additionally, the difference in local control between T1 tumors and T2/T3 tumors was also significant, with a higher local control rate observed for T1 tumors. There were no significant differences in local control between

Table 3.7: **Results from the multivariate analysis quantifying the effect of near minimum and near maximum dose accuracy on the risk of local failure while controlling for PTV volume, clinical T stage, and/or tumor location.**

	Model adjusted for:							
	PTV Volume		Clinical T-Stage		Tumor Location		PTV Volume & Tumor Location	
Dose-Volume Metric	HR (95% CI)	p-value	HR (95% CI)	p-value	HR (95% CI)	p-value	HR (95% CI)	p-value
PTV D1% BED	0.90 (0.81-1.00)	0.059	0.89 (0.78-1.01)	0.080	0.91 (0.81-1.02)	0.11	0.92 (0.82-1.02)	0.12
PTV D99% BED	1.0 (0.94-1.07)	0.92	1.0 (0.93-1.08)	0.97	1.01 (0.95-1.07)	0.76	1.0 (0.95-1.06)	0.91
ITV D1% BED	0.89 (0.79-0.99)	0.039	0.88 (0.77-1.0)	0.056	0.89 (0.79-1.01)	0.065	0.90 (0.81-1.01)	0.077
ITV D99% BED	0.99 (0.92-1.05)	0.64	0.98 (0.92-1.05)	0.56	0.99 (0.94-1.06)	0.84	0.99 (0.93-1.05)	0.63

Abbreviations: PTV = planning target volume; ITV = internal target volume; BED = biologically effective dose; HR = hazard ratio; CI = confidence interval.

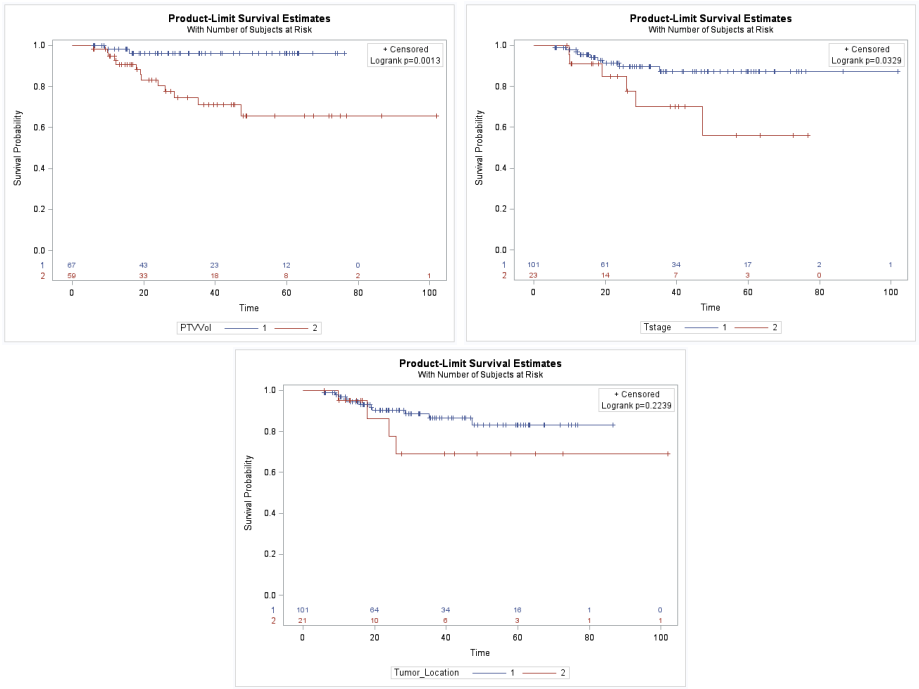

Figure 3.5: **KM curves showing the difference in local failure rates for patients stratified by PTV volume, clinical T-stage, and tumor location.**

centrally and peripherally located lesions.

3.4 Discussion

Previous studies evaluating the accuracy of different dose calculation algorithms in the presence of heterogeneity show type A algorithms to be less accurate and reliable than type B or C algorithms [22, 23, 27]. The results of this study are consistent with the findings of those studies. Our data also shows consistency with previous studies evaluating the differences between type B and type C algorithms in heterogeneous media [29, 32, 33, 48, 57]. The differences between algorithms can be substantial depending on the anatomy of the patient and the treatment technique. For example, larger lung volumes and treatments utilizing higher beam energies are likely to experience larger dosimetric differences when using more accurate algorithms.

The studies by Latifi [58] and Ohri [60] show a clear dependence of local failure on the dose calculation algorithm used for treatment planning. However, these studies did not quantify the

effects the magnitude of the dosimetric uncertainties after recalculation with more accurate algorithms have on the risk of local failure. Rather, they compared two different treatment arms, one of which was planned using a type A algorithm and the other using a more advanced algorithm. The study by Zhuang et al. [61] showed there to be no significant differences in the delivered doses between local failures and local controls when the original treatment plans were recalculated with more accurate algorithms. However, the patients in those studies were planned to the same nominal prescription dose, which was not the case in this study. Differing prescription doses leads to different delivered doses, so calculating the magnitude of the dosimetric changes relative to the original value is more appropriate for plans with variable prescription doses.

This data shows a wide variety of uncertainty present in the delivered dose when the clinically delivered treatment plans utilized type A or type B algorithms. The dosimetric uncertainties alone do not necessarily correlate with local failure. There were a handful of patients who were controlled but had large dosimetric changes upon recalculation with AXBm. For example, some patients may have experienced a significant decrease in BED when their treatment plan was recalculated with AXBm but the TCP remained high (see Fig. 3.3) due to factors related to the tumor size. Although most of the investigated parameters were not well correlated with local failure, we did see significant HRs in the UVA for the dosimetric change in the PTV and ITV D1% BEDs. When PTV volume was controlled for in the MVA, the hazard ratio associated with the change in the ITV D1% BED remained significant. However, all other hazard ratios were not statistically significant in the MVA, although a few were approaching the level of significance. While PTV volume and clinical T-stage ought to be well correlated, they are defined in different ways. T-stage is often defined from diagnostic imaging studies and other clinical examinations while the PTV volume is defined from the planning CT, which inherently takes in to account the unique PTV margin and motion management technique used for each patient.

While the change in most of the dose metrics investigated were not well correlated with local failure, Table 3.5 shows that most of the investigated dose metrics were, on average, lower for the patients who failed locally compared to patients who were controlled. This was seen in both the clinical data and the AXBm data. Lower BEDs have been shown to lead to increased rates of local

recurrence in SBRT for NSCLC [68, 69]. The prescription dose in lung SBRT is highly limited by the irradiated volume and proximity to OARs. The size of the irradiated volume directly impacts lung toxicity due to the parallel nature of the lungs. Parallel organs are known to experience volume effects. As with any other radiation therapy treatments, doses to normal tissues must be minimized in order to prevent normal tissue toxicities. Therefore, patients with larger tumors or tumors close to other OARs may have lower BEDs simply by proximity to OARs, all in an effort to minimize the likelihood of developing adverse side effects.

2 of the 15 failure cases were originally planned with PBC, which raises the question whether or not these patients would have failed had they been originally planned with AAA. Figure 3.1 indicates a wide variation in calculated dose when recalculating the PBC plans with AAA. The doses calculated using AAA were always less than PBC, which means had the plans been planned with AAA they likely would have been closer to the AXBm calculations, making the magnitude of the dosimetric change decrease. Whether or not this would have affected the treatment outcome is unknown.

Doses reported from AAA and PBC in the TPS have historically been dose-to-water [49, 50] (representing different tissues as water composition with varying density defined by the CT data). However, AXB inherently reports dose as dose-to-medium but is also able to report in terms of dose-to-water using a post-processing step. Because our analysis included dose-to-water calculations for the AAA and PBC plans, we felt it appropriate to report dose-to-medium but do a comparison to verify similarities in the reporting methods for the AXB calculations. The differences between the two reporting methods in the AXB calculations were very small. The differences have been shown to be more pronounced in higher density structures (like bone), but the small differences between the reporting methods observed in this study are consistent with previous studies [32, 51]. This could potentially be an issue for a peripherally located lesion which has the potential to include ribs and/or spine as part of the PTV. However, no large differences were noted in our analysis. A recent review published by Kry et al. [50] recommends reporting dose-to-medium when possible.

This work primarily investigated uncertainties in the BED in order to intercompare fractionation schedules, a quantity which is derived from the LQ model of cell killing. However, the validity

of the LQ model in lung SBRT has been questioned [64]. Higher doses per fraction tend to overestimate the biological effects of common SBRT doses. The traditional LQ model would require higher doses in order to eradicate all hypoxic tumor cells and effectively control the tumor [70]. Since the BED is derived from the LQ model, the BED calculations may not be reflective of the true radiobiological response of NSCLC treated with SBRT. Despite the skepticism, SBRT doses used clinically have been shown to provide excellent tumor control rates [71]. There has been some evidence of enhanced indirect cell killing with highly hypofractionated doses due to damage to tumor vasculature and enhanced tumor immunity [65, 70, 72]. This enhanced indirect cell killing causes less of a deviation from the classical LQ model. While damage to tumor vasculature will negatively impact tumor reoxygenation, this is likely to be accompanied by a rapid decrease in the oxygen consumption rate, which allows for adequate reoxygenation [70].

One limitation to this study is that follow-up times were not consistent across the patient cohort and the dataset was not complete. While patients with little to no follow-up were omitted from failure analysis, differences in follow-up times between the patients who failed and patients who were controlled could adversely affect the outcome analysis. Potential local failure cases may have been lost for patients who did not have extensive follow-up (extending beyond 2-3 years) or for patients who died within this timeframe. However, patients who died without failure were treated as a competing event. Omitting patients without extensive follow-up from suvival analysis could potentially bias the results because it would exclude patients who live far away or patients who struggle getting to follow-up appointments. These inherent uncertainties are common in retrospective outcome studies, but nonetheless patients without extensive follow up were considered in the survival analysis.

3.5 Conclusions

SBRT is a very effective treatment for early-stage NSCLC. The dose calculation algorithms currently used clinically can introduce uncertainty in the delivered dose. In this analysis, AXBm was in better agreement with Monte Carlo calculations than was AAA for lung SBRT. The clini-

cally delivered treatment plans showed a wide range of dosimetric uncertainty when the plans were recalculated with AXBm for both failure and control cases. Factors influencing the magnitude of the dosimetric change upon recalculation with AXBm included beam energy, lung volume, and the average PTV density. Most of the dosimetric changes observed were not well correlated with local failure, but the change in the PTV and ITV near maximum doses were found to be associated with local failure in the UVA.

Bibliography

[1] A. Fogliata, G. Nicolini, E. Vanetti, A. Clivio, P. Winkler, and L. Cozzi. The impact of photon dose calculation algorithms on expected dose distributions in lungs under different respiratory phases. *Physics in Medicine and Biology*, 53(9):2375–2390, 2008.

[2] A. Ahnesjö, M. Saxner, and A. Trepp. A pencil beam model for photon dose calculation. *Medical Physics*, 19(2):263–273, 1992.

[3] T. Nyholm, J. Olofsson, A. Ahnesjö, and M. Karlsson. Photon pencil kernel parameterisation based on beam quality index. *Radiotherapy and Oncology*, 78:347–351, 2006.

[4] B. Liang, Y. Li, B. Liu, F. Zhou, S. Xu, and Q. Wu. A pencil beam dose calculation model for CyberKnife system. *Medical Physics*, 43:5380–5391, 2016.

[5] P. Almond, P. Biggs, B. Coursey, W. Hanson, M. Huq, R. Nath, and D. Rogers. AAPM's TG-51 protocol for clinical reference dosimetry of high-energy photon and electron beams. *Medical Physics*, 26:1847–1870, 1999.

[6] T. Nyholm, J. Ologsson, A. Ahnesjö, and M. Karlsson. Modelling lateral beam quality variations in pencil kernel based photon dose calculations. *Physics in Medicine and Biology*, 51:4111–4118, 2006.

[7] T. Mackie, J. Scrimger, and J. Battista. A convolution method of calculating dose for 15-MV x rays. *Medical Physics*, 12:188–196, 1985.

[8] N. Papanikolaou, T. Mackie, C. Meger-Wells, M. Gehring, and P. Reckwerdt. Investigation of the convolution method for polyenergetic spectra. *Medical Physics*, 20:1327–1336, 1993.

[9] W. Ulmer, J. Pyyry, and W. Kaissl. A 3D photon superposition/convolution algorithm and its foundation on results of Monte Carlo calculations. *Physics in Medicine and Biology*, 50(8):1767–1790, 2005.

[10] O. Vassiliev, T. Wareing, J. McGhee, G. Failla, M. Salehpour, and F. Mourtada. Validation of a new grid-based Boltzmann equation solver for dose calculation in radiotherapy with photon beams. *Physics in Medicine and Biology*, 55:581–598, 2010.

[11] J. Bedford. Calculation of absorbed dose in radiotherapy by solution of the linear Boltzmann transport equations. *Physics in Medicine and Biology*, 64(2), 2019.

[12] Y. Liang, W. Muhammad, G. Hart, B. Nartowt, Z. Chen, J. Yu, K. Roberts, J. Duncan, and J. Deng. A general-purpose Monte Carlo particle transport code based on inverse transform sampling for radiotherapy dose calculation. *Scientific Reports*, 10(1), 2020.

[13] Lung cancer - non-small cell - statistics, 2021.

[14] What is lung cancer?, 2021.

[15] R. Rosen and A. Sapra. TNM Classification. 2021.

[16] H. West, E. Valliéres, and S. Schild. Management of stage I and stage II non-small cell lung cancer - UpToDate. 2021.

[17] J. Heinzerling and R. Timmerman. Stereotactic body radiation therapy for lung tumors - UpToDate. 2021.

[18] R. Ginsberg and L. Rubinstein. Randomized trial of lobectomy versus limited resection for T1 N0 non-small cell lung cancer. *The Annals of Thoracic Surgery*, 1995.

[19] B. Sun, E. Brooks, R. Komaki, Z. Liao, M. Jeter, M. McAleer, P. Allen, P. Balter, J. Welsh, M. O'Reilly, D. Gomez, S. Hahn, J. Roth, R. Mehran, J Heymach, and J. Chang. 7-year follow-up after stereotactic ablative radiotherapy for patients with stage I non-small cell lung cancer: Results of a phase 2 clinical trial. *Cancer*, 123(16):3031–3039, 2017.

[20] Y. Nagata, M. Hiraoka, T. Shibata, H. Onishi, M. Kokubo, K. Karasawa, Y. Shioyama, R. Onimaru, T. Kozuka, E. Kunieda, T. Saito, K. Nakagawa, M. Hareyama, Y. Takai, K. Hayakawa, N. Mitsuhashi, and S. Ishikura. Prospective trial of stereotactic body radiation therapy for both operable and inoperable T1N0M0 non-small cell lung cancer: Japan Clinical Oncology Group Study JCOG0403. *International Journal of Radiation Oncology Biology Physics*, 93(5):989–996, 2015.

[21] B. Ackerson, B. Tong, J. Hong, L. Gu, J. Chino, J. Trotter, T. D'Amico, J. Torok, K. Lafata, C. Chang, and C. Kelsey. Stereotactic body radiation therapy versus sublobar resection for stage I NSCLC. *Lung Cancer*, 125:185–191, 2018.

[22] A. Fogliata, E. Vanetti, D. Albers, C. Brink, A. Clivio, T. Knöös, G. Nicolini, and L. Cozzi. On the dosimetric behaviour of photon dose calculation algorithms in the presence of simple geometric heterogeneities: Comparison with Monte Carlo calculations. *Physics in Medicine and Biology*, 52(5):1363–1385, 2007.

[23] P. Carrasco, N. Jornet, M. Duch, L. Weber, M. Ginjaume, T. Eudaldo, D. Jurado, A. Ruiz, and M. Ribas. Comparison of dose calculation algorithms in phantoms with lung equivalent heterogeneities under conditions of lateral electronic disequilibrium. *Medical Physics*, 31(10):2899–2911, 2004.

[24] L. Aarup, A. Nahum, C. Zacharatou, T. Juhler-Nøttrup, T. Knöös, H. Nyström, L. Specht, E. Wieslander, and S. Korreman. The effect of different lung densities on the accuracy of various radiotherapy dose calculation methods: Implications for tumour coverage. *Radiotherapy and Oncology*, 91(3):405–414, 2009.

[25] Y. Tsuruta, M. Nakata, M. Nakamura, Y. Matsuo, K. Higashimura, H. Monzen, T. Mizowaki, and M. Hiraoka. Dosimetric comparison of Acuros XB, AAA, and XVMC in stereotactic body radiotherapy for lung cancer. *Medical Physics*, 41(8), 2014.

[26] T. Knöös, A. Ahnesjo, P. Nilsson, and L. Weber. Limitations of a pencil beam approach to photon dose calculations in lung. *Physics in Medicine and Biology*, 40(9):1411–1420, 1995.

[27] I. Lax, V. Panettieri, B. Wennberg, M. Duch, I. Näslund, P. Baumann, and G. Gagliardi. Dose distributions in SBRT of lung tumors: Comparison between two different treatment planning

algorithms and Monte-Carlo simulation including breathing motions. *Acta Oncologica*, pages 978–988, 2006.

[28] B. Dobler, C. Walter, A. Knopf, D. Fabri, R. Loeschel, M. Polednik, F. Schneider, F. Wenz, and F. Lohr. Optimization of extracranial stereotactic radiation therapy of small lung lesions using accurate dose calculation algorithms. *Radiation Oncology*, 1, 2006.

[29] A. Fogliata and L. Cozzi. Dose calculation algorithm accuracy for small fields in non-homogeneous media: The lung SBRT case. *Physica Medica*, 44:157–162, 2017.

[30] J. Ojala, M. Kapanen, S. Hyödynmaa, T. Wigren, and M. Pitkänen. Performance of dose calculation algorithms from three generations in lung SBRT: comparison with full Monte Carlo-based dose distributions. *Radiation Oncology*, 15(2), 2014.

[31] J. Seppala, S. Suilamo, J. Kulmala, P. Mali, and H. Minn. A dosimetric phantom study of dose accuracy and build-up effects using IMRT and RapidArc in stereotactic irradiation of lung. *Radiation Oncology*, 7(79), 2012.

[32] A. Fogliata, G. Nicolini, A. Clivio, E. Vanetti, and L. Cozzi. Dosimetric evaluation of Acuros XB advanced dose calculation algorithm in heterogeneous media. *Radiation Oncology*, 6(1), 2011.

[33] A. Ananda, G. Babu, A. Giri, B. Alagar, G. Mani, and K. Karunakaran. Percentage depth dose calculation accuracy of model based algorithms in high energy photon small fields through heterogeneous media and comparison with plastic scintillator dosimetry. *Journal of Applied Clinical Medical Physics*, 17(1), 2016.

[34] O. Calvo, A. Gutiérrez, S. Stathakis, C. Esquivel, and N. Papanikolaou. On the quantification of the dosimetric accuracy of collapsed cone convolution superposition (CCCS) algorithm for small lung volumes using IMRT. *Journal of Applied Clinical Medical Physics*, 13:43–59, 2012.

[35] J. Chow, M. Leung, and J. Van Dyk. Variations of lung density and geometry on inhomogeneity correction algorithms: A Monte Carlo dosimetric evaluation. *Medical Physics*, 36(8):3619–3630, 2009.

[36] N. Hardcastle, B. Oborn, and A. Haworth. On the use of a convolution-superposition algorithm for plan checking in lung stereotactic body radiation therapy. *Journal of Applied Clinical Medical Physics*, 17(5):99–110, 2016.

[37] B. Huang, L. Wu, P. Lin, and C. Chen. Dose calculation of Acuros XB and Anisotropic Analytical Algorithm in lung stereotactic body radiotherapy treatment with flattening filter free beams and the potential role of calculation grid size. *Radiation Oncology*, 10(1), 2015.

[38] W. Luo, A. Meacham, X. Xie, J. Li, P. Aryal, R. McGarry, and J. Molloy. Monte Carlo dose verification for lung SBRT with CMS/XiO superposition algorithm. *Biomedical Physics and Engineering Express*, 2, 2016.

[39] W. Mampuya, M. Nakamura, Y. Hirose, K. Kitsuda, T. Ishigaki, T. Mizowaki, and M. Hiraoka. Difference in dose-volumetric data between the Analytical Anisotropic Algorithm, the dose-to-medium, and the dose-to-water reporting modes of the Acuros XB for lung stereotactic body radiation therapy. *Journal of Applied Clinical Medical Physics*, 17(5):341–347, 2016.

[40] S. Kry, P. Alvarez, A. Molineu, C. Amador, J. Galvin, and D. Followill. Algorithms used in heterogeneous dose calculations show systematic differences as measured with the radiological physics center's anthropomorphic thorax phantom used for RTOG credentialing. *International Journal of Radiation Oncology Biology Physics*, 85(1), 2013.

[41] A. Bezjak, R. Paulus, L. Gaspar, R. Timmerman, W. Straube, W. Ryan, Y. Garces, A. Pu, A. Singh, G. Videtic, R. McGarry, P. Iyengar, J. Pnatarotto, J. Urbanic, A. Sun, M. Daly, I. Grills, P. Sperduto, D. Normolle, J. Bradley, and H. Choy. Safety and efficacy of a five-fraction stereotactic body radiotherapy schedule for centrally located non-small cell lung cancer: NRG Oncology/RTOG 0813 trial. *Journal of Clinical Oncology*, 37(15):1316–1325, 2019.

[42] G. Videtic, R. Paulus, A. Singh, J. Chang, W. Parker, K. Olivier, R. Timmerman, R. Komaki, J. Urbanic, K. Stephans, S. Yom, C. Robinson, C. Belani, P. Iyengar, M. Ajlouni, D. Gopaul, J. Gomez Suescun, R. McGarry, H. Choy, and J. Bradley. Long-term follow-up on NRG OncologyRTOG 0915 (NCCTG N0927): A randomized phase 2 study comparing 2 stereotactic body radiation therapy schedules for medically inoperable patients with stage I peripheral non-small cell lung cancer. *International Journal of Radiation Oncolgoy Biology Physics*, 103(5):1077–1084, 2019.

[43] T. Lacornerie, A. Lisbona, X. Mirabel, E. Lartigau, and N. Reynaert. GTV-based prescription in SBRT for lung lesions using advanced dose calculation algorithms. *Radiation Oncology*, 103(5), 2019.

[44] J. Li, J. Galvin, A. Harrison, R. Timmerman, Y. Yu, and Y. Xiao. Dosimetric verification using Monte Carlo calculations for tissue heterogeneity-corrected conformal treatment plans following RTOG 0813 dosimetric criteria for lung cancer stereotactic body radiotherapy. *International Journal of Radiation Oncology Biology Physics*, 84(2):508–513, 2012.

[45] D. Pokhrel, R. Badkul, H. Jiang, P. Kumar, and F. Wang. Technical note: Dosimetric evaluation of Monte Carlo algorithm in iPlan for stereotactic ablative body radiotherapy (SABR for lung cancer patients using RTOG 0813 parameters). *Journal of Applied Clinical Medical Physics*, 16(1):349–359, 2015.

[46] D. Pokhrel, S. Sood, R. Badkul, H. Jiang, C. McClinton, C. Lominska, P. Kumar, and F. Wang. Assessment of Monte Carlo algorithm for compliance with RTOG 0915 dosimetric criteria in peripheral lung cancer patients treated with stereotactic body radiotherapy. *Journal of Applied Clinical Medical Physics*, 17:277–293, 2016.

[47] S. Rana, K. Rogers, S. Pokharel, and C. Cheng. Evaluation of Acuros XB algorithm on RTOG 0813 dosimetric criteria for SBRT lung treatment with RapidArc. *Journal of Applied Clinical Medical Physics*, 15(1):118–129, 2014.

[48] C. Zhou, N. Bennion, R. Ma, X. Liang, S. Wang, K. Zvolanek, M. Hyun, X. Li, S. Zhou, W. Zhen, C. Lin, A. Wahl, and D. Zheng. A comprehensive dosimetric study on switching from a Type-B to a Type-C dose algorithm for modern lung SBRT. *Radiation Oncology*, 12(1), 2017.

[49] S. Kry, V. Feygelman, P. Balter, T. Knöös, C. Charlie Ma, M. Snyder, B. Tonner, and O. Vassiliev. AAPM task group 329: Reference dose specification for dose calculations: Dose-to-water or dose-to-muscle? *Medical Physics*, 47(3):52–64, 2020.

[50] S. Kry, J. Lye, C. Clark, N. Andratschke, A. Dimitriadis, D. Followhill, R. Howell, M. Hussein, M. Ishikawa, S. Kito, T. Kron, J. Lee, J. Michalski, A. Filippo Monti, N. Reynaert, P. Taylor, K. Venables, Y. Xiao, and J. Lehmann. Report dose-to-medium in clinical trials where available; a consensus from the global HARMONISATION group to maximize consistency. *Radiotherapy and Oncology*, 2021.

[51] C. Munoz-Monteplet, R. Fuentes-Raspall, D. Jurado-Bruggeman, S. Agramunt-Chaler, A. Onsés-Segarra, and M. Buxó. Dosimetric impact of Acuros XB dose-to-water and dose-to-medium reporting modes on lung stereotactic body radiation therapy and its dependency on structure composition. *Advances in Radiation Oncology*, 2021.

[52] A. Sahgal, V. Weinberg, L. Ma, E. Chang, S. Chao, A. Muacevic, A. Gorgulho, S. Soltys, P. Gerszten, S. Ryu, L. Angelov, I. Gibbs, C. Wong, and D. Larson. Probabilities of radiation myelopathy specific to stereotactic body radiation therapy to guide safe practice. *International Journal of Radiation Oncology Biology Physics*, 85(2):341–347, 2013.

[53] R. Barriger, J. Forquer, J. Brabham, D. Andolino, R. Shapiro, M. Henderson, P. Johnstone, and A. Fakiris. A dose-volume analysis of radiation pneumonitis in non-small cell lung cancer patients treated with stereotactic body radiation therapy. *International Journal of Radiation Oncology Biology Physics*, 82(1):457–462, 2012.

[54] J. Forquer, A. Fakiris, R. Timmerman, S. Lo, S. Perkins, R. McGarry, and P. Johnstone. Brachial plexopathy from stereotactic body radiotherapy in early-stage NSCLC: dose-limiting toxicity in apical tumor sites. *International Journal of Radiation Oncology Biology Physics*, 93(3), 2009.

[55] B. Hoppe, B. Laser, A. Kowalski, S. Fontenla, E. Pena-Greenberg, E. Yorke, D. Lovelock, M. Hunt, and K. Rosenzweig. Acute skin toxicity following stereotactic body radiation therapy for Stage I non-small cell lung cancer: Who's at risk? *International Journal of Radiation Oncology Biology Physics*, 72(5), 2008.

[56] N. Dunlap, J. Cai, G. Biedermann, W. Yang, S. Benedict, K. Sheng, T. Schefter, B. Kavanagh, and J. Larner. Chest wall volume receiving $>$30 Gy predicts risk of severe pain and/or rib fracture after lung stereotactic body radiotherapy. *International Journal of Radiation Oncology Biology Physics*, 76(3):796–801, 2010.

[57] C. Ong, K. Ang, R. Soh, K. Tin, J. Yap, J. Lee, and C. Bragg. Dosimetric comparison of peripheral NSCLC SBRT using Acuros XB and AAA calculation algorithms. *Medical Dosimetry*, 42(3):216–222, 2017.

[58] K. Latifi, J. Oliver, R. Baker, T. Dilling, C. Stevens, J. Kim, B. Yue, M. Demarco, G. Zhang, E. Moros, and V. Feygelman. Study of 201 non-small cell lung cancer patients given stereotactic ablative radiation therapy shows local control dependence on dose calculation algorithm. *International Journal of Radiation Oncology Biology Physics*, 88(5), 2014.

[59] J. Song, K. Kang, H. Choi, H. Jeong, I. Ha, J. Lee, H. Kim, Y. Jeong, Y. Cho, S. Lee, S. Kim, I. Jang, and B. Jeong. Comparing the clinical outcomes in stereotactic body radiotherapy for lung tumors between Ray-Tracing and Monte-Carlo algorithms. *Oncotarget*, 7(14), 2016.

[60] M. Ohri, W. Tomé, S. Kalnicki, and M. Garg. Stereotactic body radiation therapy for stage I non-small cell lung cancer: The importance of treatment planning algorithm and evaluation of a tumor control probability model. *Practical Radiation Oncology*, 8(2):e33–e39, 2018.

[61] T. Zhuang, N. Woody, H. Liu, S. Cherian, C. Reddy, P. Qi, A. Magnelli, T. Djemil, K. Stephans, P. Xia, and G. Videtic. Dosimetric differences between local failure and local controlled non-small cell lung cancer patients treated with stereotactic body radiotherapy: A matched-pair study. *Journal of Medical Imaging and Radiation Oncology*, 62(3):420–424, 2018.

[62] V. Murali, P. Gopalakrishna Kurup, N. Bhuvaneswari, H. Sudahar, and M. Muthukumaran. Monte Carlo and ray tracing algorithms in the CyberKnife treatment planning for lung tumours - comparison and validation. *Journal of Radiosurgery and SBRT*, 2013.

[63] Eric Hall and Amato Giaccia. *Radiobiology for the Radiologist*. Lippincott Williams & Wilkins, a Wolters Kluwer Business, Philadelphia, 2012.

[64] R. Klement, J. Sonke, M. Allgäuer, N. Andratschke, S. Appold, J. Belderbos, C. Belka, K. Dieckmann, H. Eich, M. Flentje, I. Grills, M. Eble, A. Hope, A. Grosu, S. Semrau, R. Sweeney, J. Hörner-Rieber, M. Werner-Wasik, R. Engenhart-Cabillic, H. Ye, and M. Guckenberger. Estimation of the α/β ratio of non-small cell lung cancer treated with stereotactic body radiotherapy. *Radiotherapy and Oncology*, 142:210–216, 2020.

[65] J. Brown, D. Carlson, and D. Brenner. The tumor radiobiology of SRS and SBRT: Are more than the 5 Rs involved? *International Journal of Radiation Oncology Biology Physics*, 88(2):254–262, 2014.

[66] S. Piffer, M. Casati, L. Marrazzo, C. Arilli, S. Calusi, I. Desideri, F. Fusi, S. Pallotta, and C. Talamonti. Validation of a secondary dose check tool against Monte Carlo and analytical dose calculation algorithms in VMAT. *Journal of Applied Clinical Medical Physics*, 2021.

[67] J. Fine and R. Gray. A proportional hazards model for the subdistribution of a competing risk. *Journal of the American Statistical Association*, 94(446):496–509, 1999.

[68] H. Onishi, T. Araki, H. Shirato, Y. Nagata, M. Hiraoka, K. Gomi, T. Yamashita, Y. Niibe, K. Karasawa, K. Hayakawa, Y. Takai, T. Kimura, Y. Hirokawa, A. Takeda, A. Ouchi, M. Hareyama, M. Kokubo, R. Hara, J. Itami, and K. Yamada. Stereotactic hypofractionated high-dose irradiation for stage I non-small cell lung carcinoma: Clinical outcomes in 245 subjects in a Japanese multi-institutional study. *Cancer*, 101(7):1623–1631, 2004.

[69] A. Moreno, B. Fellman, B. Hobbs, Z. Liao, D. Gomez, A. Chen, S. Hahn, J. Chang, and S. Lin. Biologically effective dose in stereotactic body radiotherapy and survival for patients with early-stage NSCLC. *Journal of Thoracic Oncology*, 15(1):101–109, 2020.

[70] M. Kim, W. Kim, I. Park, H. Kim, E. Lee, J. Jung, L. Cho, and C. Song. Radiobiological mechanisms of stereotactic body radiation therapy and stereotactic radiation surgery. *Radiation Oncology Journal*, 33(4):265–275, 2015.

[71] P. Lee, B. Loo, T. Biswas, G. Ding, I. El Naqa, A. Jackson, F. Kong, T. LaCouture, M. Miften, T. Solberg, W. Tome, A. Tai, E. Yorke, and X. Li. Local control after stereotactic body radiation therapy for stage I non-small cell lung cancer. *International Journal of Radiation Oncology Biology Physics*, 110(1):160–171, 2021.

[72] C. Song, E. Glatstein, L. Marks, B. Emami, J. Grimm, P. Sperduto, M. Kim, S. Hui, K. Dusenbery, and L. Cho. Biological principles of stereotactic body radiation therapy (SBRT) and stereotactic radiation surgery (SRS): Indirect cell death. *International Journal of Radiation Oncology Biology Physics*, 110(1):21–34, 2021.

[73] T. Mitin, J. Loeffler, and S. Vora. Radiation therapy techniques in cancer treatment - UpToDate. 2021.

[74] C. Chen, P. Chapman, and J. Loeffler. Stereotactic cranial radiosurgery. 2021.

[75] M. Ghaly, E. Gogineni, and M. Saif. The evolving field of stereotactic body radiation therapy in pancreatic cancer. *Pancreas - Open Journal*, 3(1):9–14, 2019.

[76] H. Hijazi, M. Campeau, D. Roberge, D. Donath, R. Lapointe, F. Vandenbroucke-Menu, D. Taussky, K. Boudam, G. Chan, A. Bujold, and G. Delouya. Stereotactic body radiotherapy for inoperable liver tumors: Results of a single institutional experience. *Cureus*, 8(12), 2016.

[77] K. Vuolukka, P. Auvinen, E. Tiainen, J. Palmgren, J. Heikkilä, J. Seppälä, S. Aaltomaa, and V. Kataja. Stereotactic body radiotherapy for localized prostate cancer - 5-year efficacy results. *Radiation Oncology*, 15(1), 2020.